ARMY RESEARCH LABORATORY

Uniaxial Crushing of Sandwich Plates Under Air Blast: Influence of Mass Distribution

by Joseph A. Main and George A. Gazonas

ARL-RP-210 **June 2008**

A reprint from the *International Journal of Solids and Structures*, vol. 45, pp. 2297–2321, 2008.

NOTICES

Disclaimers

The findings in this report are not to be construed as an official Department of the Army position unless so designated by other authorized documents.

Citation of manufacturer's or trade names does not constitute an official endorsement or approval of the use thereof.

Destroy this report when it is no longer needed. Do not return it to the originator.

Army Research Laboratory
Aberdeen Proving Ground, MD 21005-5069

ARL-RP-210 **June 2008**

Uniaxial Crushing of Sandwich Plates Under Air Blast: Influence of Mass Distribution

Joseph A. Main
National Institute of Standards and Technology

George A. Gazonas
Weapons and Materials Research Directorate, ARL

A reprint from the *International Journal of Solids and Structures*, vol. 45, pp. 2297–2321, 2008.

REPORT DOCUMENTATION PAGE

Form Approved
OMB No. 0704-0188

1. REPORT DATE *(DD-MM-YYYY)*	2. REPORT TYPE	3. DATES COVERED (From - To)
June 2008	Reprint	April 2005 – October 2007

4. TITLE AND SUBTITLE
Uniaxial Crushing of Sandwich Plates Under Air Blast: Influence of Mass Distribution

5a. CONTRACT NUMBER

5b. GRANT NUMBER

5c. PROGRAM ELEMENT NUMBER

6. AUTHOR(S)
Joseph A. Main and George A. Gazonas

5d. PROJECT NUMBER
62105AH84

5e. TASK NUMBER

5f. WORK UNIT NUMBER

7. PERFORMING ORGANIZATION NAME(S) AND ADDRESS(ES)
U.S. Army Research Laboratory
ATTN: AMSRD-ARL-WM-MD
Aberdeen Proving Ground, MD 21005-5069

8. PERFORMING ORGANIZATION REPORT NUMBER
ARL-RP-210

9. SPONSORING/MONITORING AGENCY NAME(S) AND ADDRESS(ES)

10. SPONSOR/MONITOR'S ACRONYM(S)

11. SPONSOR/MONITOR'S REPORT NUMBER(S)

12. DISTRIBUTION/AVAILABILITY STATEMENT
Approved for public release; distribution is unlimited.

13. SUPPLEMENTARY NOTES
A reprint from the *International Journal of Solids and Structures*, vol. 45, pp. 2297–2321, 2008.

14. ABSTRACT
Motivated by recent efforts to mitigate blast loading using energy-absorbing materials, this report uses analytical and computational modeling to investigate the influence of mass distribution on the uniaxial crushing of cellular sandwich plates under air blast loading. In the analytical model, the cellular core is represented using a rigid, perfectly-plastic, locking idealization, as in previous studies, and the front and back faces are modeled as rigid, with pressure loading applied to the front face and the back-face unrestrained. This model is also applicable to the crushing of cellular media in ‘‘blast pendulum’’ experiments. Fluid–structure interaction effects are treated using a recent result that accounts for nonlinear compressibility effects for intense air blasts. Predictions of the analytical model show excellent agreement with explicit finite element computations, and the model is used to investigate the response of the system for all possible distributions of mass between the front and back faces and the cellular core. Increasing the mass fraction in the front face is found to increase the impulse required for complete crushing of the cellular core but also to produce undesirable increases in back-face accelerations. Optimal mass distributions for mitigating shock transmission through the sandwich plate are investigated by maximizing the impulse capacity while limiting the back-face accelerations to a specified level.

15. SUBJECT TERMS
air blast, metallic foams, optimization, finite elements, sandwich plates, LS-DYNA, fluid-structure interaction

16. SECURITY CLASSIFICATION OF:			17. LIMITATION OF ABSTRACT	18. NUMBER OF PAGES	19a. NAME OF RESPONSIBLE PERSON
a. REPORT	b. ABSTRACT	c. THIS PAGE			George Gazonas
UNCLASSIFIED	UNCLASSIFIED	UNCLASSIFIED	UL	36	19b. TELEPHONE NUMBER (*Include area code*) 410-306-0863

Available online at www.sciencedirect.com
ScienceDirect
International Journal of Solids and Structures 45 (2008) 2297–2321
INTERNATIONAL JOURNAL OF SOLIDS AND STRUCTURES
www.elsevier.com/locate/ijsolstr

Uniaxial crushing of sandwich plates under air blast: Influence of mass distribution ☆

Joseph A. Main [a,*], George A. Gazonas [b]

[a] National Institute of Standards and Technology, Building and Fire Research Laboratory, 100 Bureau Drive, Stop 8611, Gaithersburg, MD 20899-8611, USA
[b] US Army Research Laboratory, Weapons and Materials Research Directorate ATTN: AMSRD-ARL-WM-MD, Aberdeen Proving Ground, MD 21005-5069, USA

Received 13 October 2006; received in revised form 11 October 2007
Available online 8 December 2007

Abstract

Motivated by recent efforts to mitigate blast loading using energy-absorbing materials, this paper uses analytical and computational modeling to investigate the influence of mass distribution on the uniaxial crushing of cellular sandwich plates under air blast loading. In the analytical model, the cellular core is represented using a rigid, perfectly-plastic, locking idealization, as in previous studies, and the front and back faces are modeled as rigid, with pressure loading applied to the front face and the back-face unrestrained. This model is also applicable to the crushing of cellular media in ''blast pendulum'' experiments. Fluid–structure interaction effects are treated using a recent result that accounts for nonlinear compressibility effects for intense air blasts. Predictions of the analytical model show excellent agreement with explicit finite element computations, and the model is used to investigate the response of the system for all possible distributions of mass between the front and back faces and the cellular core. Increasing the mass fraction in the front face is found to increase the impulse required for complete crushing of the cellular core but also to produce undesirable increases in back-face accelerations. Optimal mass distributions for mitigating shock transmission through the sandwich plate are investigated by maximizing the impulse capacity while limiting the back-face accelerations to a specified level.
Published by Elsevier Ltd.

Keywords: Sandwich plates; Metallic foams; Fluid–structure interaction; Finite elements; Optimization; Air blast

1. Introduction

Sandwich plates with cellular metal cores are being widely considered for blast-mitigation applications, due largely to the energy absorption capacity of the cellular core material. Computational simulations have shown

☆ Disclaimer: Certain trade names or company products are mentioned in the text to specify adequately the procedure used. Such identification does not imply recommendation or endorsement by NIST or ARL, nor does it imply that the product is the best available for the purpose.

* Corresponding author. Tel.: +1 301 975 5286; fax: +1 301 869 6275.
E-mail addresses: joseph.main@nist.gov (J.A. Main), gazonas@arl.army.mil (G.A. Gazonas).

0020-7683/$ - see front matter Published by Elsevier Ltd.
doi:10.1016/j.ijsolstr.2007.11.019

that under blast loading, sandwich plates exhibit reduced deflections relative to solid plates with the same total mass (Xue and Hutchinson, 2003, 2004; Fleck and Deshpande, 2004; Qiu et al., 2004; Hutchinson and Xue, 2005; Vaziri and Hutchinson, 2006). These studies considered identical face sheets, and while the influence of varying the mass ratio between the face sheets and the core has been studied, the influence of varying the mass ratio between the two face sheets has not. The influence of varying the thickness of the face sheet nearest the blast, in particular, is not obvious, because two competing effects are at work. On the one hand, reducing the thickness of this front face means that the blast impulse is imparted to a smaller mass, resulting in increased kinetic energy, which must be dissipated through crushing of the core. This effect was noted by Xue and Hutchinson (2004) in a computational study of blast loading on sandwich plates, in which the kinetic energy imparted to a sandwich plate was observed to be greater than for a monolithic solid plate of the same total mass. On the other hand, reducing the front face thickness enhances the beneficial effects of fluid–structure interaction (FSI), which leads to reductions in the impulse imparted to the system. A recent study that accounted for nonlinear compressibility effects in air blast loading on freestanding solid plates found that such impulse reductions due to FSI could be fairly significant (Kambouchev et al., 2006), more significant than predicted by the linear acoustic FSI analysis of Taylor (1963), which has been used in previous analyses of blast loading on sandwich plates. Depending which of these effects is dominant, benefits might be achieved by either increasing or decreasing the mass fraction in the face sheet nearest the blast.

Motivated by these observations, this paper uses analytical and computational modeling to investigate the influence of mass distribution on the uniaxial crushing of sandwich plates under air blast, considering all possible distributions of mass between the two face sheets and the cellular core. While previous studies of blast loading on sandwich plates have primarily focused on minimizing dynamic deflections, the main interest in the present study is in mitigating shock transmission through the thickness of the sandwich plate. A potential application is for shock isolation of electronic components mounted to the back face of an armor panel. Accelerations of the back face are of particular concern in such applications, because damage to an electronic component is related to the acceleration transmitted to its base.

Because stress–strain curves for cellular media exhibit a characteristic plateau, it has been noted (Hanssen et al., 2002) that a cellular layer could potentially serve a protective function against blast loading by limiting the stresses transmitted through the layer to the plateau stress σ_P. However, this protective function is lost if complete densification of the cellular layer is permitted, in which case the transmitted stresses can actually be amplified. Such amplification can occur because the crushing mechanism of cellular media under blast or high-speed impact involves propagation of a densification front with the characteristics of a shock wave. While the stress ahead of the densification front is limited to the plateau stress, a velocity-dependent jump in stress across the densification front can result much higher stress in the crushed material behind the densification front. This stress enhancement due to shock formation has been exploited in the use of metal foam projectiles to simulate shock loading on structures (Rathbun et al., 2006; Radford et al., 2006). Under blast loading, stresses several times larger than the peak applied blast pressure can be transmitted through a cellular layer if the thickness of the layer is insufficient to arrest the densification front, as observed by Li and Meng (2002).

This mechanism of stress enhancement due to shock formation helps to account for the surprising observation that the use of cellular materials under blast loading has in many instances led to enhancement, rather than mitigation, of blast effects. Cooper et al. (1991) reported enhanced thoracic injury in animals whose chest cavities were "protected" by a foam layer, and computational studies conducted by Friend (2005) revealed that thoracic injury is exacerbated by shock wave compression of alternating soft foam layers and subsequent acceleration of more rigid layers in porous foam body armor. Experiments by Hanssen et al. (2002) showed that increased upswing resulted from the addition of an aluminum foam layer to the face of a massive "pendulum" subjected to blast loading, and other examples of enhanced blast effects are described by Li and Meng (2002). In discussing the blast pendulum experiments of Hanssen et al. (2002), Nesterenko (2002) credited the observed impulse enhancement to the first of the two competing effects mentioned above, noting that the blast impulse would have been imparted primarily to a lightweight plate covering the foam layer, leading to significantly higher kinetic energy than if the same impulse were imparted directly to the more massive pendulum. Nesterenko (2002) suggested that complete crushing could then lead to detachment and rebounding of the densified foam layer, thus increasing the resultant momentum of the pendulum. It is noted that the blast pendulum can be considered an extreme example of a "sandwich plate" with unequal face sheets, with most of the

mass in the back face (i.e., the pendulum) and relatively small masses in the front face and the cellular core. The present study can thus afford insights into the influence of mass distribution on the poor performance of this system under blast loading.

To investigate the influence of mass distribution on the uniaxial crushing of sandwich plates under air blast loading, an analytical model is developed in this paper in which the front and back faces are treated as rigid, with a pressure pulse applied to the front face and the back-face unrestrained, and the cellular core is represented using the well-established rigid, perfectly-plastic, locking (R-P-P-L) continuum idealization. The R-P-P-L idealization was originally developed to model the dynamic crushing of wood (Reid and Peng, 1997) and has subsequently been applied to metal honeycombs and foams in a number of studies (Harrigan et al., 1999; Hanssen et al., 2002; Tan et al., 2005b). The R-P-P-L idealization can be applied to a variety of cellular topologies, provided that the cell dimensions are sufficiently small relative to the domain of interest to justify the continuum approximation. Based on impact experiments for aluminum foams, Tan et al. (2005a) observed that the domain of interest should include at least five average cell diameters for a valid continuum approximation. For cases in which the cell sizes are large and the individual core elements are relatively stocky, representing the core crushing as a planar densification front propagating through a continuum may be inappropriate, and the core crushing may be better represented using the model developed by Vaughn et al. (2005), which considers coupled plastic wave propagation and nonlinear buckling of individual columns. Xue and Hutchinson (2006) showed that the model of Vaughn et al. (2005) predicted quite accurately the dynamic crushing strength of square honeycomb sandwich cores under different crushing rates. While the R-P-P-L idealization does not explicitly incorporate rate dependence in the plateau stress, rate-dependent behavior results from the shock wave formation and the associated velocity-dependent stress jump mentioned previously. Tan et al. (2005a, Fig. 18), showed that a one-dimensional shock model using the R-P-P-L idealization was able to accurately predict experimental observations of increasing crushing stress with increasing impact velocity for aluminum foam projectiles.

As illustrated in Fig. 1, a number of previous studies have developed analytical models to represent the one-dimensional crushing of cellular media under various dynamic loading conditions. Reid and Peng (1997) used the R-P-P-L idealization to model the dynamic crushing of wood cylinders impacting a rigid wall, obtaining an expression for the enhancement of stress transmitted to the rigid wall as a consequence of the stress jump across the shock front. This model was subsequently applied to aluminum honeycomb projectiles by Harrigan et al. (1999). Hanssen et al. (2002) investigated the crushing of a metal foam bar with a triangular pressure pulse applied to a rigid cover sheet, comparing finite element results with an analytical solution using the R-P-P-L idealization. They obtained an expression for the minimum thickness required to fully absorb a given impulse, thereby limiting the stress transmitted to the rigid support to the plateau stress σ_P. Li and Meng

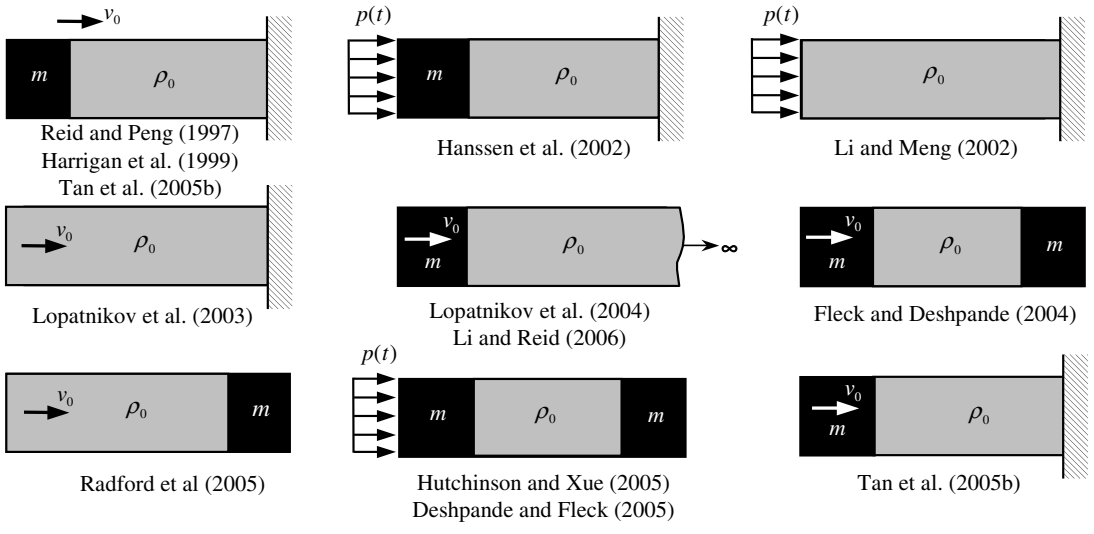

Fig. 1. One-dimensional systems considered in previous studies.

(2002) used a nonlinear spring-mass model to examine the shock wave propagation through a cellular medium subject to a rectangular pressure pulse, and as noted previously, they observed a sharp increase in the stress transmitted to the rigid support for impulses exceeding the energy absorption capacity of the cellular layer. The R-P-P-L idealization was extended by Lopatnikov et al., 2003, 2004, who used an elastic, perfectly-plastic, rigid (E-P-P-R) idealization to model the dynamic deformation of metal foam materials under both Taylor impact and plate impact boundary conditions. Li and Reid (2006) subsequently proposed corrections to the unloading assumption used in the E-P-P-R model and the impact velocity regimes defined by Lopatnikov et al. (2003) for the plate impact problem.

In analyzing the dynamic response of sandwich beams and plates to blast loading, Fleck and Deshpande (2004) and Hutchinson and Xue (2005) divided their analyses into three temporal stages, of which stage I involved FSI in the reflection of the incident pressure pulse from the front face of the sandwich panel, and stage II involved one-dimensional compaction of the cellular core with initial velocities resulting from the stage I analysis. Both studies treated FSI in stage I by applying the linear acoustic analysis of Taylor (1963) to the front face, while Hutchinson and Xue (2005) extended this analysis to incorporate the resistance provided by a perfectly-plastic core. Both studies analyzed the core crushing in stage II by employing a quasi-static assumption for the energy dissipation in the core, with Fleck and Deshpande (2004) employing the R-P-P-L idealization and Hutchinson and Xue employing a perfectly-plastic idealization with no compaction limit. In a subsequent analysis of shock wave propagation in cellular media, however, Radford et al. (2005) noted that the energy dissipation in the core could be significantly larger than the quasi-static value because of additional dissipation within the shock wave. This additional dissipation is associated with a drop in kinetic energy across the shock front, which follows from the balance of momentum, not from an explicit assumption of material rate dependence. Assuming a linear rate dependence for the cellular material, Radford et al. (2005) presented an asymptotic analysis of the shock structure, which enabled a quantification of the viscous dissipation that balances the drop in kinetic energy. Tan et al. (2005b) also noted the incorrectness of a global energy balance that assumes quasi-static energy dissipation in the core, using a thermo-mechanical approach to derive the governing equations for shock propagation in an R-P-P-L solid and showing that quasi-static assumption leads to a contradiction. The velocity-dependent energy dissipation associated with the shock front was properly accounted for in a more recent model developed by Deshpande and Fleck (2005) for one-dimensional crushing of sandwich plates. This model also relaxed the requirement of a strict temporal separation between FSI in stage I and core crushing in stage II by considering time-varying loading on the front face rather than simply applying the resulting impulse to the front face as an initial velocity.

In terms of the representation of shock wave propagation and associated energy dissipation in the cellular core, the present model is equivalent to that of Deshpande and Fleck (2005), although it was developed independently and was previously reported briefly in Main and Gazonas (2005). Key differences are that Deshpande and Fleck (2005) considered face sheets of equal mass, while the present model allows for arbitrary masses of the front and back faces, and that Deshpande and Fleck (2005) used the linear acoustic analysis of Taylor (1963) to represent FSI effects for underwater shock loading, while the present model incorporates the recent analysis of Kambouchev et al. (2006) to account for nonlinear compressibility and FSI effects in air-blast loading. Vaziri and Hutchinson (2006) presented two approaches for implementing the result of Kambouchev et al. (2006) in computational simulations of sandwich plates under air-blast loading, one in which the reflected impulse is imparted to the front face through an initial velocity and another in which a time-dependent pressure history is applied to the front face. The present study uses a modification of the latter approach that accounts for the initial resistance provided by the plateau stress of the cellular core.

The outline of this paper is as follows. The derivation of the analytical model is first presented in Section 2, and in Section 3 predictions of the analytical model are compared with finite element results. Initiation and arrest of densification are considered in Section 4, in which the analytical model is used to investigate the influence of mass distribution on the critical reflected impulse required for complete densification of the cellular core under different levels of peak reflected pressure. The influence of mass distribution on the time required for complete densification and the corresponding energy dissipation in the core are also investigated. FSI effects are considered in Section 5, in which the influence of mass distribution on the critical *incident* impulse is investigated and the work done by the air blast on the sandwich plate is compared with the work done on a corresponding solid plate with the same total mass. Finally, accelerations of the back face are investigated in

Section 6, and optimal mass distributions for mitigation of shock transmission are investigated by seeking to maximize the impulse that can be absorbed while limiting the back-face accelerations to a specified level.

2. Analytical model

A strip through the thickness of a sandwich plate is considered, as depicted with a partially compacted core in Fig. 2a. The R-P-P-L idealization, depicted in Fig. 2b, is used to represent the stress–strain relationship of the core material. The applied pressure pulse $p_r(t)$ is the pressure reflected from the front face of the sandwich panel and is influenced by the nonlinear compressibility of air and by fluid–structure interaction (FSI). Because of FSI effects, p_r actually depends on the motion of the front face and cannot be formally defined as a function solely of time t. However, Section 5 presents an approximate approach, based on the analysis of Kambouchev et al. (2006), whereby nonlinear compressibility and FSI effects are accounted for in defining a reflected pressure pulse $p_r(t)$ that results from a specified incident pressure pulse $p_i(t)$. While no particular functional form is assumed for $p_r(t)$ in the derivation of the analytical model, it is assumed that the peak reflected pressure p_R occurs initially, so that $p_r(0) = p_R$ and $p_r(t) \leqslant p_R$ for $t > 0$.

2.1. Equation of motion

A strip of sandwich plate with unit cross-sectional area is considered (i.e., with unit area exposed to the blast pressure), with total mass given by $m = m_1 + \rho_0\ell_0 + m_2$, where ρ_0 and ℓ_0 are the uncompressed density and initial thickness of the cellular core, and m_1 and m_2 are the areal densities of the front and back faces, respectively. The acceleration of the center of mass, denoted $\ddot{u}_G$, follows directly from application of Newton's second law to the entire system, whereby all internal forces cancel and the time derivative of the net momentum is equivalent to the net external force (because a strip of unit cross-sectional area is considered, forces and pressures can be used interchangeably):

$$p_r(t) = m\ddot{u}_G \tag{1}$$

The total momentum of the system can be obtained by integrating Eq. (1) with respect to time, assuming that the panel is initially at rest, $\dot{u}_G(0) = 0$, to give the impulse–momentum relationship

$$i_r(t) = m\dot{u}_G \tag{2}$$

where $i_r(t)$ denotes the reflected impulse per unit area:

$$i_r(t) = \int_0^t p_r(\hat{t})\mathrm{d}\hat{t} \tag{3}$$

Provided that the applied pressure is sufficiently high, densification of the cellular core commences at the front face, and a shock front propagates through the core. (The pressure required to initiate densification is investigated subsequently.) According to the simplified model of Fig. 2b, the densified core material moves as a rigid body with the same velocity as the front face, while the uncompressed core material moves as a rigid body with the velocity of the back face. Since the motion of the center of mass is known from Eqs. (1) and (2), it is convenient to express the positions of the front and back faces of the panel with reference to the position of the mass center, as follows:

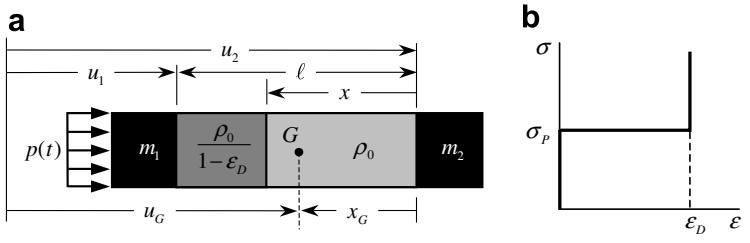

Fig. 2. Analytical model definition: (a) strip of sandwich panel with partially compacted core and (b) engineering stress–strain relationship for cellular core material (R-P-P-L idealization).

$$u_1 = u_G - (\ell - x_G); \quad u_2 = u_G + x_G \tag{4a, b}$$

where u_1 and u_2 denote the positions of the front and back faces, respectively, ℓ denotes the total thickness of the core, and x_G denotes the distance from the center of mass to the back face, as shown in Fig. 2a. With ε_D denoting the volumetric strain at complete densification, it follows from conservation of mass that the density of the compressed core material is $\rho_0/(1-\varepsilon_D)$ and the total thickness of the core is given by

$$\ell = \ell_0 - \varepsilon_D(\ell_0 - x) \tag{5}$$

where x denotes the thickness of the uncompressed core material, and the thickness of the shock front itself is assumed to be negligible. By forming and differentiating an expression for x_G the following relation can be obtained:

$$\dot{x}_G = (\varepsilon_D/m)[m_1 + \rho_0(\ell_0 - x)]\dot{x} \tag{6}$$

The following expressions for the velocities of the front and back faces can then be obtained by differentiating Eqs. (4a,b) and (5) and combining with Eq. (6):

$$\dot{u}_1 = [i_r(t) - \varepsilon_D(\rho_0 x + m_2)\dot{x}]/m; \quad \dot{u}_2 = \{i_r(t) + \varepsilon_D[m_1 + \rho_0(\ell_0 - x)]\dot{x}\}/m \tag{7a, b}$$

in which the substitution $\dot{u}_G = i_r(t)/m$ from Eq. (2) has been made.

The stress just ahead of the shock front is σ_P, and application of Newton's second law to the material ahead of the shock front yields the following equation:

$$\sigma_P = (\rho_0 x + m_2)\ddot{u}_2 \tag{8}$$

Differentiating Eq. (7b) and substituting into Eq. (8) then yields the following nonlinear ordinary differential equation for x:

$$-\varepsilon_D[m_1 + \rho_0(\ell_0 - x)]\ddot{x} + \varepsilon_D\rho_0\dot{x}^2 = p_r(t) - \sigma_P m/(\rho_0 x + m_2) \tag{9}$$

Eq. (9) can be integrated numerically with initial conditions $x(0) = \ell_0$ and $\dot{x}(0) = 0$.

2.2. Energy balance

The balance of mechanical energy for the system of Fig. 2 requires that the work done by the pressure pulse, denoted W_p, must equal the sum of the kinetic energy of the system, denoted E_k, and the energy dissipated in the core material, denoted E_d:

$$W_p = E_k + E_d \tag{10}$$

The work per unit area done by the pressure pulse can be expressed as follows, in terms of the applied pressure $p_r(t)$ and the velocity of the front face $\dot{u}_1$:

$$W_p = \int_0^t p_r(\hat{t})\dot{u}_1 \, d\hat{t} \tag{11}$$

The expression for $\dot{u}_1$ from Eq. (7b) can then be substituted into Eq. (11). The resulting integral contains the term $i_r(\hat{t})p_r(\hat{t})$, which integrates directly to $\frac{1}{2}i_r^2(t)$, yielding the following expression:

$$W_p = \frac{1}{2}i_r^2(t)/m - (\varepsilon_D/m)\int_0^t p_r(\hat{t})(\rho_0 x + m_2)\dot{x} \, d\hat{t} \tag{12}$$

The first term in Eq. (12) represents the work done by the pressure pulse if no densification occurs ($\dot{x} = 0$), in which case the front face moves at the same velocity as the center of mass, $\dot{u}_1 = \dot{u}_G$. The second term in Eq. (12) represents the enhancement of this work resulting from densification of the cellular core. This term is positive because $\dot{x} < 0$ as the shock front propagates. Densification of the core results in larger velocities of the front face ($\dot{u}_1 > \dot{u}_G$), so that the applied pressure acts through a larger distance, resulting in increased work.

With the thickness of the shock front assumed negligible, the kinetic energy of the sandwich panel per unit area can be expressed as follows, as the sum of contributions from the portions on each side of the shock front:

$$E_{\mathrm{k}} = \frac{1}{2}[m_1 + \rho_0(\ell_0 - x)]\dot{u}_1^2 + \frac{1}{2}(\rho_0 x + m_2)\dot{u}_2^2 \tag{13}$$

Substituting the expressions for $\dot{u}_1$ and $\dot{u}_2$ from Eqs. (7a,b) and collecting terms yields the following expression for the kinetic energy:

$$E_{\mathrm{k}} = \frac{1}{2}i_{\mathrm{r}}^2(t)/m + \frac{1}{2}(\varepsilon_0^2/m)[m_1 + \rho_0(\ell_0 - x)](\rho_0 x + m_2)\dot{x}^2 \tag{14}$$

The first term in Eq. (14) represents the kinetic energy associated with motion of the mass center and is equivalent to the first term in Eq. (12). The second term in Eq. (14) is zero if no densification occurs ($\dot{x} = 0$), and it represents an enhancement of the kinetic energy resulting from relative motion of the front and back faces.

Because the uncompressed material ahead of the shock front and the densified material behind the shock front are both assumed to act rigidly, it is only within the shock front that energy dissipation occurs. An expression for the energy dissipated in the core can then be obtained by considering a control volume that encloses the shock front. With the thickness of the shock front assumed negligible, no mass or kinetic energy can accumulate within the control volume. Therefore, the flux of kinetic energy into the control volume must be balanced by the rate of external work on the control volume and the rate of energy dissipation within the control volume. The rate of energy dissipation within the control volume can then be expressed as follows:

$$\dot{E}_{\mathrm{d}} = \frac{1}{2}\rho_0(\dot{u}_1 - \dot{u}_2)(\dot{u}_2^2 - \dot{u}_1^2)/\varepsilon_{\mathrm{D}} - \sigma_{\mathrm{P}}\dot{u}_2 + (\sigma_{\mathrm{P}} + \Delta\sigma)\dot{u}_1 \tag{15}$$

The first term on the right-hand side gives the flux of kinetic energy into the control volume, where $\rho_0(\dot{u}_1 - \dot{u}_2)/\varepsilon_{\mathrm{D}}$ gives the flux of mass through the control volume, $\frac{1}{2}\dot{u}_2^2$ represents the kinetic energy per unit mass entering the control volume, and $\frac{1}{2}\dot{u}_1^2$ represents the kinetic energy per unit mass leaving the control volume. The remaining terms give the net rate of external work on the system within the control volume. The quantity $\Delta\sigma$ represents the jump in stress across the shock front, and it follows from conservation of momentum that $\Delta\sigma$ is given by

$$\Delta\sigma = \rho_0(\dot{u}_2 - \dot{u}_1)^2/\varepsilon_{\mathrm{D}} \tag{16}$$

Substituting Eq. (16) into Eq. (15) and collecting terms yields the following expression:

$$\dot{E}_{\mathrm{d}} = -\sigma_{\mathrm{P}}(\dot{u}_2 - \dot{u}_1) - \frac{1}{2}\rho_0(\dot{u}_2 - \dot{u}_1)^3/\varepsilon_{\mathrm{D}} \tag{17}$$

Noting that $u_2 - u_1 = \ell$, it follows from differentiation of Eq. (5) that $\dot{u}_2 - \dot{u}_1 = \varepsilon_{\mathrm{D}}\dot{x}$, whereby Eq. (17) can be expressed in terms of $\dot{x}$ as

$$\dot{E}_{\mathrm{d}} = -\sigma_{\mathrm{P}}\varepsilon_{\mathrm{D}}\dot{x} - \frac{1}{2}\rho_0\varepsilon_{\mathrm{D}}^2\dot{x}^3 \tag{18}$$

With the conditions $E_{\mathrm{d}} = 0$ and $x = \ell_0$ at $t = 0$, Eq. (18) can then be integrated to give

$$E_{\mathrm{d}} = \sigma_{\mathrm{P}}\varepsilon_{\mathrm{D}}(\ell_0 - x) - \frac{1}{2}\rho_0\varepsilon_{\mathrm{D}}^2\int_0^t \dot{x}^3\,\mathrm{d}t \tag{19}$$

The first term in Eq. (19) represents the quasi-static energy dissipation associated with densification of the core under a constant stress σ_{P}, while the second term represents a rate-dependent enhancement of energy dissipation associated with the shock front.

It is noted that the equation of motion (9) can be derived in an alternative manner by using the work and energy expressions presented in this section. Differentiation of Eq. (10) with respect to time yields the following relationship:

$$\dot{W}_{\mathrm{p}} = \dot{E}_{\mathrm{k}} + \dot{E}_{\mathrm{d}} \tag{20}$$

It can then be readily verified that differentiation of Eqs. (12), (14), and (19) and substitution into Eq. (20) yields the same differential equation as Eq. (9). The equation of motion (9) is therefore fully consistent with the mechanical energy balance presented in this section.

2.3. Nondimensionalization

For the sake of generality, it is useful to express the equation of motion (9) in terms of nondimensional quantities. A nondimensional coordinate ξ is introduced to denote the position of the shock front:

$$\xi = x/\ell_0 \tag{21}$$

It is noted that ξ represents the remaining mass fraction of uncompressed core material and that $\xi = 1$ initially. The symbol i_R is introduced to denote the total reflected impulse per unit area:

$$i_R = \int_0^\infty p_r(t)\mathrm{d}t \tag{22}$$

so that $i_r(t) \to i_R$ as $t \to \infty$. A nondimensional time τ can be defined as follows:

$$\tau = t\sigma_P/i_R \tag{23}$$

The derivatives of the shock front position x can then be expressed in terms of nondimensional variables as $\dot{x} = (\ell_0\sigma_P/i_R)\mathrm{d}\xi/\mathrm{d}\tau$ and $\ddot{x} = (\ell_0\sigma_P^2/i_R^2)\mathrm{d}^2\xi/\mathrm{d}\tau^2$. A nondimensional reflected pressure $P_r(\tau)$ can also be defined as a function of nondimensional time through division of $p_r(t)$ by the plateau stress σ_P and a change of variables using Eq. (23):

$$P_r(\tau) = \left.\frac{p_r(t)}{\sigma_P}\right|_{t=\tau i_R/\sigma_P} \tag{24}$$

For convenience in numerical solution, the additional state variable $\upsilon = \mathrm{d}\xi/\mathrm{d}\tau$ is introduced, which represents the nondimensional relative velocity of the shock front, whereby the equation of motion can be recast as a first-order differential equation in vector form as follows:

$$\frac{\mathrm{d}}{\mathrm{d}\tau}\begin{Bmatrix}\xi\\ \upsilon\end{Bmatrix} = \begin{Bmatrix}\upsilon\\ \dfrac{-I_R^2[P_r(\tau)-(\eta_0\xi+\eta_2)^{-1}]+\eta_0^2\upsilon^2}{\eta_0\eta_1+\eta_0^2(1-\xi)}\end{Bmatrix} \tag{25}$$

where I_R is a nondimensional total impulse, defined as

$$I_R = \frac{i_R}{m}\sqrt{\frac{\rho_0}{\sigma_P\varepsilon_D}} \tag{26}$$

and η_0, η_1, and η_2 represent the fractions of the total mass in the core, the front face, and the back face, respectively:

$$\eta_0 = \rho_0\ell_0/m; \quad \eta_1 = m_1/m; \quad \eta_2 = m_2/m \tag{27}$$

For a given form of the pressure input $P_r(\tau)$, Eq. (25) can be integrated numerically with the initial conditions $\xi(0) = 1$ and $\upsilon(0) = 0$, corresponding to initially uncrushed foam.

Once time histories of ξ and υ have been obtained by numerical integration, it is necessary to express the response quantities of interest in terms of these nondimensional state variables and the nondimensional pressure $P_r(\tau)$. Nondimensional front-face and back-face velocities can be defined as follows:

$$\tilde{v}_1 = \frac{\dot{u}_1}{i_R/m}; \quad \tilde{v}_2 = \frac{\dot{u}_2}{i_R/m} \tag{28a,b}$$

where i_R/m is the limiting velocity of the center of mass as $t \to \infty$, which follows from Eqs. (2) and (22). By substituting Eqs. (7a,b) into Eqs. (28a,b) the following expressions can be obtained:

$$\tilde{v}_1 = I_r(\tau) - \frac{\eta_0^2\xi + \eta_0\eta_2}{I_R^2}\upsilon; \quad \tilde{v}_2 = I_r(\tau) + \frac{\eta_0^2(1-\xi) + \eta_0\eta_1}{I_R^2}\upsilon \tag{29a,b}$$

where $I_r(\tau)$ is a nondimensional impulse defined as follows, so that $I_r(\tau) \to 1$ as $t \to \infty$:

$$I_r(\tau) = \int_0^\tau P_r(\hat{\tau})\mathrm{d}\hat{\tau} = \left.\frac{i_r(t)}{i_R}\right|_{t=\tau i_R/\sigma_P} \tag{30}$$

The acceleration of the back-face $\ddot{u}_2$ is of interest in evaluating the protective function of the cellular core, and it follows from Eq. (8) that this is given by $\ddot{u}_2 = \sigma_0/(\rho_0 x + m_2)$. A nondimensional back-face acceleration can then be defined as follows:

$$\tilde{a}_2 = \frac{\ddot{u}_2}{\sigma_P/m} = \frac{1}{\eta_0\xi + \eta_2} \tag{31}$$

Nondimensional versions of the work and energy quantities from Section 2.2 can be defined through division by $i_R^2/(2m)$, which represents the kinetic energy associated with the center of mass in the limit as $t \to \infty$:

$$\widetilde{W}_p = \frac{W_p}{\frac{1}{2}i_R^2/m}; \quad \widetilde{E}_k = \frac{E_k}{\frac{1}{2}i_R^2/m}; \quad \widetilde{E}_d = \frac{E_d}{\frac{1}{2}i_R^2/m} \tag{32a, b, c}$$

Substituting Eq. (14) into Eq. (32b), the nondimensional kinetic energy can be expressed as follows:

$$\widetilde{E}_k = I_r^2(\tau) + (\eta_0^2/I_R^4)[\eta_1 + \eta_0(1-\xi)](\eta_2 + \eta_0\xi)v^2 \tag{33}$$

Because the expressions for W_p and E_d in Eqs. (12) and (19) contain integrals with respect to time, it is convenient to express the nondimensional quantities $\widetilde{W}_p$ and $\widetilde{E}_d$ in terms of their derivatives with respect to nondimensional time τ, as follows:

$$\frac{\mathrm{d}\widetilde{W}_p}{\mathrm{d}\tau} = 2P_r(\tau)[I_r(\tau) - (\eta_0/I_R^2)(\eta_0\xi + \eta_2)v] \tag{34}$$

$$\frac{\mathrm{d}\widetilde{E}_d}{\mathrm{d}\tau} = -(2\eta_0/I_R^2)v - (\eta_0^3/I_R^4)v^3 \tag{35}$$

In numerical solution for $\widetilde{W}_p$ and $\widetilde{E}_d$, the state vector in Eq. (25) can then be augmented to include $\widetilde{W}_p$ and $\widetilde{E}_d$, whereby Eqs. (25), (34), and (35) can be integrated simultaneously. The following expression for the nondimensional quasi-static energy dissipation, corresponding to the first term in Eq. (19), can be obtained by integrating the first term in Eq. (35):

$$\widetilde{E}_d^{q\text{-}s} = (2\eta_0/I_R^2)(1-\xi) \tag{36}$$

A nondimensional peak reflected pressure P_R can be defined as

$$P_R = p_R/\sigma_P \tag{37}$$

where $p_R = p_r(0)$ is the peak reflected pressure, assumed to occur initially. While the derivations thus far have not assumed any particular functional form for the reflected pressure pulse $p_r(t)$, the computational simulations presented in Section 3 consider a triangular pressure pulse decreasing linearly from the peak pressure p_R at $t = 0$ to zero at $t = t_R$. Using Eqs. (24) and (30), the nondimensional pressure and impulse for the triangular pulse can be expressed as follows:

$$P_r(\tau) = \begin{cases} P_R(1-\tau/\tau_R), & 0 \leqslant \tau \leqslant \tau_R \\ 0, & \tau > \tau_R \end{cases}; \quad I_r(\tau) = \begin{cases} (\tau/\tau_R)(2-\tau/\tau_R), & 0 \leqslant \tau < \tau_R \\ 1, & \tau \geqslant \tau_R \end{cases} \tag{38a, b}$$

where the nondimensional impulse duration is given by $\tau_R = t_R\sigma_P/i_R$, according to Eq. (23), and because $i_R = p_R t_R/2$ for the triangular pulse, it follows that $\tau_R = 2/P_R$.

The approximate treatment of FSI in Section 5 considers an exponential reflected pressure pulse of the form $p_r(t) = p_R\,\mathrm{e}^{-t/t_R}$, where t_R is the decay period. Using Eqs. (24) and (30), the nondimensional pressure and impulse for the exponential pulse can be expressed as follows:

$$P_r(\tau) = P_R\,\mathrm{e}^{-\tau/\tau_R}; \quad I_r(\tau) = 1 - \mathrm{e}^{-\tau/\tau_R} \tag{39a, b}$$

where $\tau_R = 1/P_R$ according to Eq. (23) with $i_R = p_R t_R$ for the exponential pulse.

The limiting case of a zero duration impulse can be considered by setting $p_r(t) = i_R\delta(t)$ and $i_r(t) = i_R H(t)$, where $\delta(t)$ is the Dirac delta function and $H(t)$ is the Heaviside step function. The nondimensional pressure and impulse in this limit are simply given by $P_r(\tau) = \delta(\tau)$ and $I_r(\tau) = H(\tau)$, respectively. By integrating the equation of motion (25) about $\tau = 0$, it can be shown that the Dirac delta pressure pulse imparts a nondimensional relative velocity of $v_0 = -I_R^2/(\eta_1\eta_0)$ to the shock front. The equation of motion (25) in this limiting case can then be solved by imposing the initial condition $v(0) = v_0$ and setting $P_r(\tau) = 0$.

3. Comparison with computational predictions

In this section, the predictions of the analytical model are compared with explicit finite element computations using LS-DYNA. The computational simulations follow fairly closely those presented by Hanssen et al. (2002), although the present study considers an unrestrained back face with different values of the front-face and back-face masses, while Hanssen et al. considered a fixed back face. In the computations, the cellular core was represented by a single row of solid elements with total thickness $\ell_0 = 5$ cm, using material model 26 (*MAT_HONEYCOMB) with $\rho_0 = 250$ kg/m^3, $\sigma_P = 1$ MPa, and $\varepsilon_0 = 0.7$. A large elastic modulus of $E = 700$ GPa was used to represent the "rigid" portions of the idealized stress–strain relationship in Fig. 2b, and Poisson's ratio was set to zero. The solid elements were defined with an initial aspect ratio of 2:1 (axial to transverse), resulting in an aspect ratio of 0.6:1 at complete densification. The front and back faces were represented in the computations by added nodal masses, and two different mass distributions were considered, as indicated in Table 1. The "blast pendulum" case corresponds to the blast pendulum experiments of Hanssen et al. (2002), with the large back-face mass representing the pendulum. The "sandwich plate" case, with equal front-face and back-face masses, corresponds to a sandwich plate as considered by Xue and Hutchinson (2003, 2004) and Fleck and Deshpande (2004).

FSI effects were not explicitly considered in the computational simulations, because the purpose of the simulations was for comparison with the crushing response predicted by the analytical model under specified reflected pressure loading. A triangular reflected pressure pulse with the form of Eq. (38a) was applied to the front face of the first solid element in the computational simulations. As shown in Table 1, a nondimensional peak reflected pressure of $P_R = 10$ was used in both the "blast pendulum" and "sandwich plate" cases, while the nondimensional impulse I_R was selected to produce comparable compaction of the core in each case, and a significantly larger value of I_R was used in the "sandwich plate" case.

As shown in Fig. 3, the computational simulations are quite sensitive to the value of the material viscosity coefficient μ specified in the material model. For the "pendulum" case with $n = 20$ elements, Fig. 3 shows that the computational simulations converge very closely to the predictions of the analytical model when μ is reduced to 0.001 Pa s, while larger values of μ result in reduced core deformation and increased values of the nondimensional back-face acceleration $\tilde{a}_2$, defined in Eq. (31). The material viscosity coefficient μ was not mentioned by Hanssen et al. (2002), but that study did find that more than 400 elements were required to achieve adequate convergence. As shown in Fig. 4, for a given value of μ the computational simulations do converge toward the predictions of the analytical model as the number of elements is increased. However, with $\mu = 0.05$ Pa s (the default value for material model 26), the computational results have not yet converged even with $n = 150$ elements, which is consistent with the observations of Hanssen et al. (2002). By reducing μ to 0.001 Pa s, adequate convergence can be achieved with fewer elements, as shown in Fig. 3. The computational results in Figs. 5 and 6 were obtained using $\mu = 0.001$ Pa s and $n = 150$ elements, which was found to be more than sufficient to achieve convergence for both the "blast pendulum" and the "sandwich plate" cases of Table 1.

Table 1
Parameters of computational simulations

Case	η_0	η_1	η_2	P_0	I_0
Blast pendulum	0.0125	0.0125	0.975	10	0.015
Sandwich plate	0.5	0.25	0.25	10	1

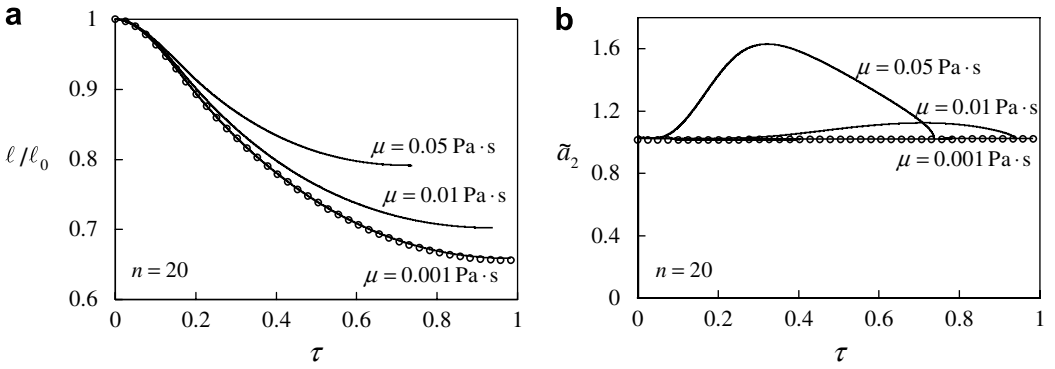

Fig. 3. Influence of material viscosity μ on convergence of computational results with $n = 20$ elements (“blast pendulum” case). (a) Nondimensional core thickness and (b) nondimensional back-face acceleration. Analytical model, ○; computational results, —.

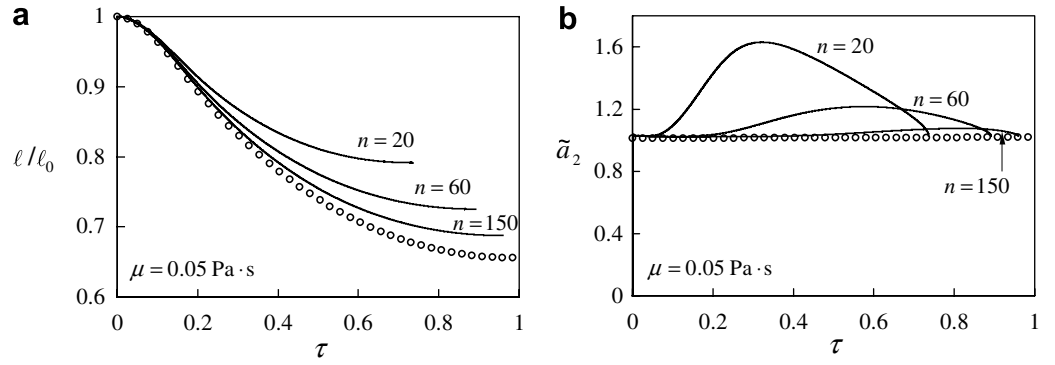

Fig. 4. Influence of number of elements n on convergence of computational results with $\mu = 0.05$ Pa s (“blast pendulum” case). (a) Nondimensional core thickness and (b) nondimensional back-face acceleration. Analytical model, ○; computational results, —.

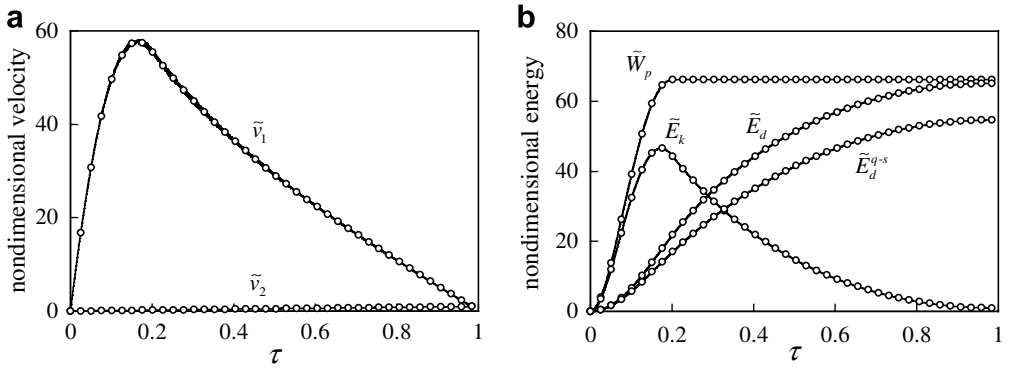

Fig. 5. Time histories of (a) nondimensional front-face and back-face velocities and (b) nondimensional energy quantities for “blast pendulum” case. Analytical model, ○; computational results, — ($n = 150$; $\mu = 0.001$ Pa s).

In Figs. 5 and 6, computational results are compared with predictions of the analytical model for the “blast pendulum” and “sandwich plate” cases, respectively, and in both cases, good agreement is observed between the analytical and computational results. Figs. 5a and 6a show the nondimensional front-face and back-face velocities defined in Eqs. (28a,b), and Figs. 5b and 6b show the nondimensional work and energy quantities defined in Eqs. (32a,b,c) and (36). All quantities are plotted against nondimensional time τ, defined in Eq. (23),

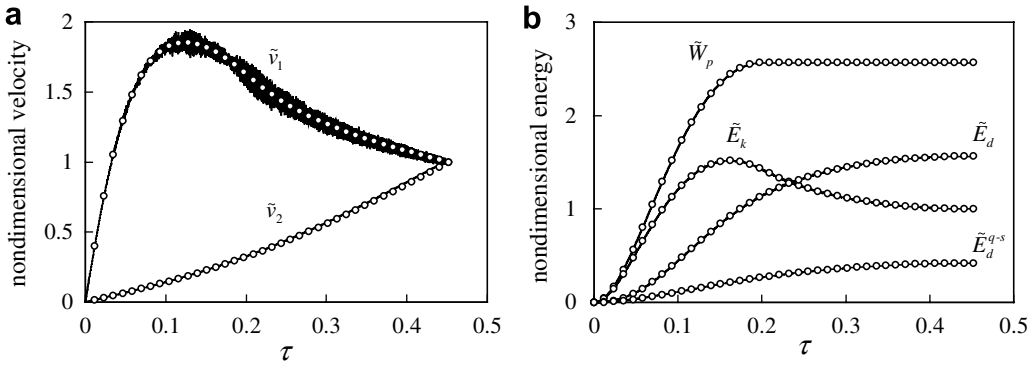

Fig. 6. Time histories of (a) nondimensional front-face and back-face velocities and (b) nondimensional energy quantities for "sandwich plate" case. Analytical model, ○; computational results, — ($n = 150$; $\mu = 0.001$ Pa s).

and all plots terminate at the instant the shock front is arrested. Beyond this instant, the entire system translates as a rigid body. At the instant the shock wave is arrested, the velocities of the front and back faces have converged, so that $\tilde{v}_1 = \tilde{v}_2 = 1$ for both the "blast pendulum" and the "sandwich plate" cases, and the nondimensional kinetic energy in both cases has plateaued at $\widetilde{E}_k = 1$. While the final value of the nondimensional front-face velocity $\tilde{v}_1$ is the same for both the "blast pendulum" and the "sandwich plate" cases, comparison of Figs. 5a and 6a shows that the peak value of $\tilde{v}_1$ is much larger in the "blast pendulum" case. The larger values of $\tilde{v}_1$ in the "blast pendulum" case are associated with much larger values of the nondimensional work done by the pressure pulse $\widetilde{W}_p$ than in the "sandwich plate" case, as seen by comparison of Figs. 5b and 6b. Figs. 5b and 6b also show that the nondimensional energy dissipation $\widetilde{E}_d$ is significantly larger than the quasi-static contribution $\widetilde{E}_d^{q\text{-}s}$ from Eq. (36), demonstrating that the rate-dependent dissipation associated with the shock front has a significant influence on the solution.

4. Initiation and arrest of densification

In order to initiate densification of the core, the peak reflected pressure p_R must be sufficiently high that the stress behind the front face reaches the plateau stress σ_P. The maximum pressure than can be sustained without densification, denoted p_R^{init}, can be evaluated by considering a free-body diagram of the front face under the applied pressure p_R^{init} with the plateau stress σ_P acting at the interface with the core. If densification has not initiated, then the acceleration of the front face must equal the acceleration of the center of mass, which is given by $\ddot{u}_G = p_R^{init}/m$ according to Eq. (1). Newton's second law for the front face can then be written as follows:

$$p_R^{init} - \sigma_P = m_1 \ddot{u}_G = m_1 (p_R^{init}/m) \tag{40}$$

Eq. (40) can be rearranged and expressed in terms of nondimensional variables, yielding the following expression for the nondimensional peak pressure required to initiate densification:

$$P_R^{init} = (1 - \eta_1)^{-1} \tag{41}$$

If $P_R > P_R^{init}$, then densification will occur, and the propagation and arrest of the shock front can be evaluated by solving the nondimensional equation of motion (25). The nondimensional time at which densification is arrested, denoted τ_A, can be evaluated as the instant that the nondimensional shock-front velocity υ reaches zero. The value of the nondimensional coordinate ξ at this instant, denoted ξ_A, gives the mass fraction of uncrushed core material remaining at arrest of densification.

Figs. 7a and b show contours of ξ_A versus P_R and I_R for the "blast pendulum" and "sandwich panel" cases, respectively (see Table 1), with a triangular pressure pulse. In both cases, the contours for $\xi_A = 1$ are horizontal lines corresponding to P_R^{init} (41), and no densification occurs for $P_R \leqslant P_R^{init}$. The contours for $\xi_A = 0$ in Figs. 7a and b correspond to complete densification of the core. For values of P_R and I_R beyond these contours, the

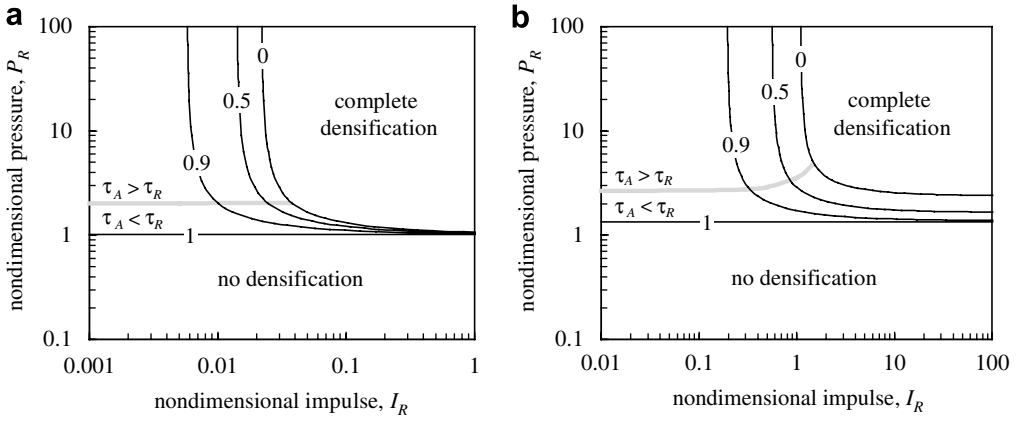

Fig. 7. Contours of remaining mass fraction of uncrushed core material ξ_A versus nondimensional reflected impulse I_R and nondimensional reflected pressure P_R (triangular pressure pulse). (a) "Blast pendulum" case and (b) "sandwich plate" case.

shock front is not arrested before reaching the back face (i.e., ξ reaches zero before v reaches zero), and the protective function of the cellular core is lost, as discussed previously. The minimum nondimensional impulse that produces complete densification of the core is denoted I_R^{crit}, and the $\xi_A = 0$ contours in Figs. 7a and b show that I_R^{crit} increases as the nondimensional peak pressure P_R decreases.

There is a minimum value of P_R for which complete densification can be achieved, which is denoted P_R^{lim}. When $P_R < P_R^{lim}$, complete densification cannot be achieved, even if the pressure is maintained indefinitely (i.e., a step function, for which $I_R \to \infty$). Values of P_R^{lim} can be evaluated numerically by selecting a very large value for I_R (a value of $I_R = 10^6$ was found to be sufficiently large) and solving Eq. (25) repeatedly with varying P_R to find the minimum value of P_R for which complete densification is achieved. In the "blast pendulum" case, $P_R^{lim} \cong 1.019$ while $P_R^{init} \cong 1.013$, and the contours for $\xi_A = 0$ and $\xi_A = 1$ in Fig. 7a are almost indistinguishable as I_R becomes large. However, in the "sandwich plate" case, $P_R^{lim} \cong 2.394$ while $P_R^{init} \cong 1.333$, and a clear gap is evident between the contours for $\xi_A = 0$ and $\xi_A = 1$ as I_R becomes large.

Plotted in grey in Figs. 7a and b are contours corresponding to $\tau_A = \tau_R$, where τ_A is the nondimensional time at which the shock front is arrested and τ_R is the nondimensional duration of the triangular reflected pressure pulse. For values of P_R and I_R below the $\tau_A = \tau_R$ contour, the shock front is arrested before the end of the pressure pulse ($\tau_A < \tau_R$), and the response is more sensitive to the peak pressure than to the total impulse. For

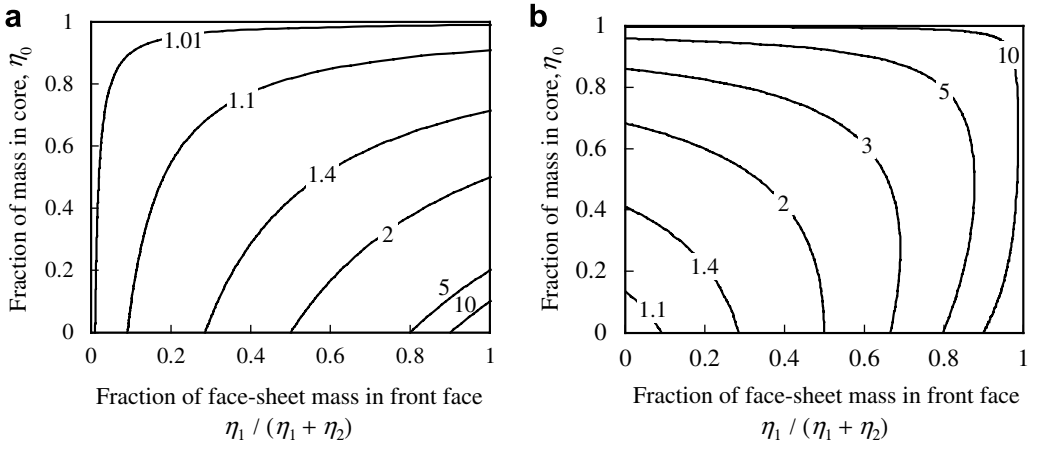

Fig. 8. Contours with varying mass distribution of (a) nondimensional reflected pressure required to initiate densification P_R^{init} and (b) minimum nondimensional reflected pressure for which complete densification of the core can be achieved P_R^{lim}.

values of P_R and I_R above the $\tau_A = \tau_R$ contours, the shock front is arrested after the end of the pressure pulse ($\tau_A > \tau_R$), and the response is more sensitive to the total impulse than to the peak pressure.

The dependence of P_R^{init} and P_R^{lim} on mass distribution is shown in Figs. 8a and b, respectively, in which contours of P_R^{init} and P_R^{lim} are plotted against the fraction of mass in the core η_0, and against the fraction of remaining mass (i.e., face-sheet mass) in the front face, $\eta_1/(\eta_1 + \eta_2)$. The remaining figures in this paper use the same axes as Fig. 8 to illustrate the influence of mass distribution on various quantities of interest. To aid in interpreting these figures, it is noted that the "sandwich plate" case corresponds to the center of these plots, with half of the mass in the core, $\eta_0 = 0.5$, and the remaining mass distributed equally between the front and back faces, $\eta_1/(\eta_1 + \eta_2) = 0.5$, while the "blast pendulum" case is near the lower left corner of these plots, with $\eta_0 = 0.0125$ and $\eta_1/(\eta_1 + \eta_2) = 0.0127$. Fig. 8 shows that both P_R^{init} and P_R^{lim} increase with increasing $\eta_1/(\eta_1 + \eta_2)$, while P_R^{init} decreases with increasing η_0. The range between P_R^{init} and P_R^{lim}, over which an infinite impulse produces only partial densification, is thus maximized in the upper right-hand corner of the plots, which corresponds to a large mass fraction in the core with most of the remaining mass in the front face.

The influence of mass distribution on I_R^{crit}, the nondimensional reflected impulse required for complete densification of the core, is shown in Figs. 9a and b, in which contours of I_R^{crit} for $P_R = 10$ and $P_R = 100$, respectively, are plotted using the same axes as in Fig. 8. For consistency with subsequent calculations that include FSI effects, the values of I_R^{crit} in Fig. 9 were computed for an exponential pressure pulse as defined in Eq. (39). It was previously observed in Fig. 7 that I_R^{crit} increases with decreasing P_R, and consequently, larger values of I_R^{crit} are observed for $P_R = 10$ (Fig. 9a) than for $P_R = 100$ (Fig. 9b). While the contours in Figs. 9a and b are fairly close over much of the plot, significant differences are observed near the right-hand edges of the plots, which correspond to a large fraction of the face-sheet mass in the front face. In Fig. 9a, a contour is plotted for $I_R^{crit} \to \infty$, which is the same as the contour for $P_R^{lim} = 10$ plotted in Fig. 8b. Along this contour, the nondimensional pressure $P_R = 10$ must be sustained indefinitely in order to achieve complete densification of the core. The shaded region beyond this contour corresponds to $P_R^{lim} > 10$, and in this region, complete densification of the core cannot be achieved with $P_R = 10$, even for an infinite impulse. Fig. 9 shows that for both $P_R = 10$ and $P_R = 100$, I_R^{crit} increases with increasing $\eta_1/(\eta_1 + \eta_2)$, and I_R^{crit} generally increases with increasing η_0, except in the lower right-hand corner of Fig. 9a, as the contour for $I_R^{crit} \to \infty$ is approached.

Figs. 10a and b show the influence of mass distribution on τ_A, the nondimensional time at which the shock front is arrested, for an exponential reflected pressure pulse with $P_R = 10$ and $P_R = 100$, respectively. Contours of τ_A/τ_R are plotted, where $\tau_R = 1/P_R$ is the nondimensional decay period of the exponential pulse. To enable a consistent comparison, since τ_A depends on I_R, the values in Figs. 10a and b were evaluated using the minimum value of I_R for which complete densification is achieved in each case (i.e., the values of I_R^{crit} shown in Figs. 9a and b, respectively). In the shaded region of Fig. 9b, for which complete densification cannot be achieved, a value of $I_R = 100$ was used. Fig. 10 shows that the values of τ_A/τ_R are about 10 times larger for

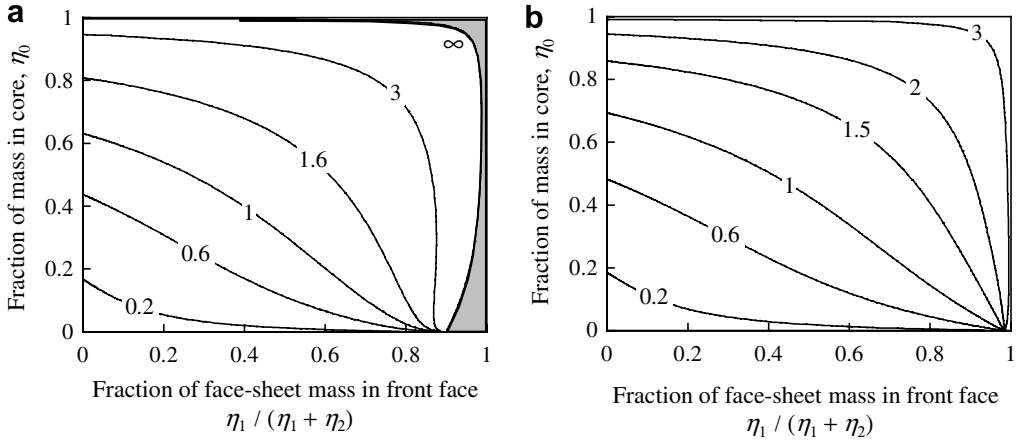

Fig. 9. Contours with varying mass distribution of nondimensional reflected impulse I_R^{crit} required for complete densification of core (exponential pressure pulse). (a) $P_R = 10$ and (b) $P_R = 100$.

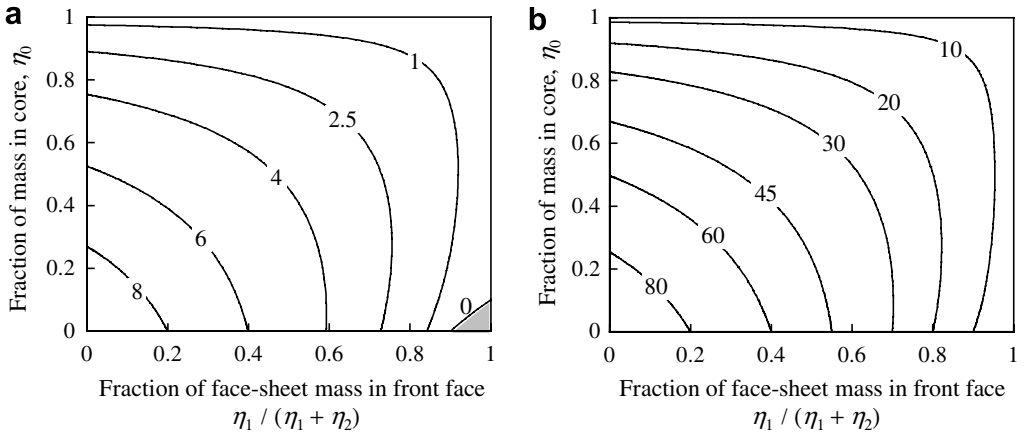

Fig. 10. Contours with varying mass distribution of the ratio τ_A/τ_R between the time of arrest of densification and the decay period of the reflected pressure pulse (values correspond to complete densification of the core, with reflected impulses shown in Fig. 9). (a) $P_R = 10$ and (b) $P_R = 100$.

$P_R = 100$ than for $P_R = 10$, as a consequence of the smaller value of τ_R in the former case. For both $P_R = 10$ and $P_R = 100$, τ_A/τ_R decreases with increasing η_0 and with increasing $\eta_1/(\eta_1 + \eta_2)$. Fig. 10a shows that in some cases $\tau_A < \tau_R$. It was observed previously in Fig. 7 that when $\tau_A < \tau_R$, the response becomes more sensitive to the peak pressure than to the total impulse. From Fig. 10a it can then be observed that when η_0 and/or $\eta_1/(\eta_1 + \eta_2)$ become large (i.e., beyond the contour for $\tau_A < \tau_R = 1$), the system becomes more sensitive to the peak pressure and less sensitive to the total impulse. In Fig. 10b a contour for $\tau_A/\tau_R = 0$ is shown, which is the same as the contour for $P_R^{init} = 10$ shown previously in Fig. 8a. In the shaded area below this contour, the nondimensional peak pressure of $P_R = 10$ is insufficient to initiate densification, regardless of the applied impulse.

Fig. 11 shows contours with varying mass distribution of the ratio $\widetilde{E}_d/\widetilde{E}_d^{q\text{-}s}$ of the total energy dissipated in the core to the quasi-static energy dissipation given by Eq. (36). As in Fig. 10, the contours in Fig. 11 correspond to complete densification of the core and were computed using the values of I_R^{crit} shown in Fig. 9, with $I_R = 100$ for cases in which complete densification cannot be achieved. Fig. 11 shows that $\widetilde{E}_d/\widetilde{E}_d^{q\text{-}s}$ increases with increasing η_0 for both $P_R = 10$ and $P_R = 100$, while significantly larger values of $\widetilde{E}_d/\widetilde{E}_d^{q\text{-}s}$ are observed

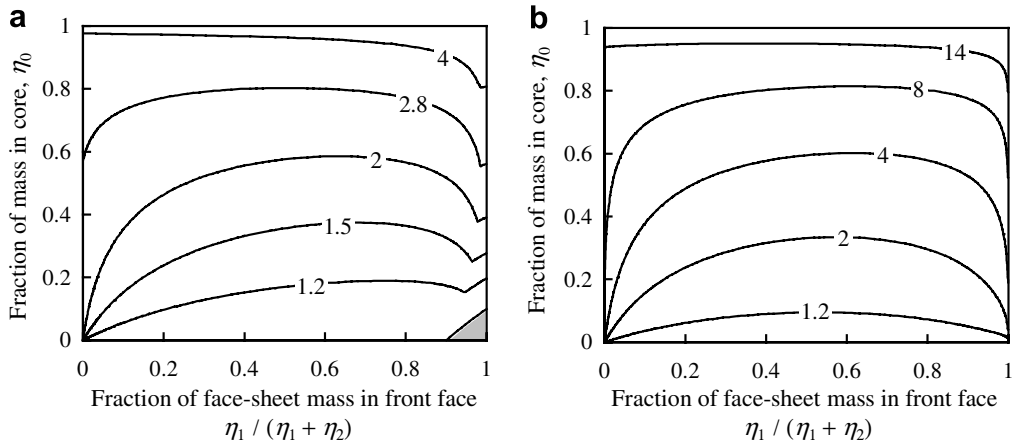

Fig. 11. Contours with varying mass distribution of the ratio $\widetilde{E}_d/\widetilde{E}_d^{q\text{-}s}$ between the total energy dissipated in the core and the quasi-static energy dissipation (values correspond to complete densification of the core, with reflected impulses shown in Fig. 9). (a) $P_R = 10$ and (b) $P_R = 100$.

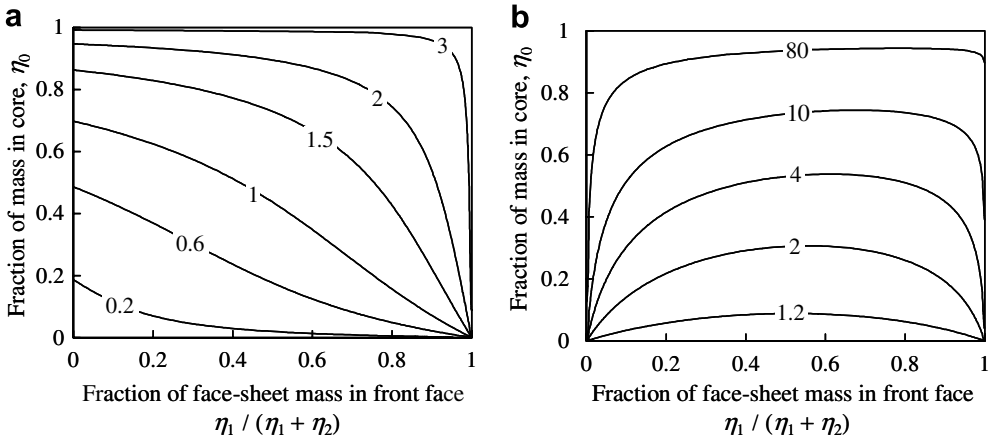

Fig. 12. Influence of mass distribution for a Dirac delta pulse ($P_R \to \infty$): contours of (a) nondimensional reflected impulse I_R^{crit} required for complete densification of core and (b) ratio $\widetilde{E}_d/\widetilde{E}_d^{q\text{-}s}$ between the total energy dissipated in the core and the quasi-static energy dissipation (values correspond to complete densification of the core, with reflected impulses shown in (a)).

for $P_R = 100$. For large η_0, the rate-dependent contribution to the energy dissipation can be many times larger than the quasi-static contribution. The shaded region in the lower right-hand corner of Fig. 11a corresponds to the shaded region in Fig. 10a, in which the nondimensional peak pressure of $P_R = 10$ is insufficient to initiate densification of the core, regardless of the applied impulse. No energy is dissipated in this region, so the ratio $\widetilde{E}_d/\widetilde{E}_d^{q\text{-}s}$ is undefined.

While Figs. 9–11 compared results for two different levels of peak pressure ($P_R = 10$ and $P_R = 100$), Fig. 12 presents results for the limiting case of a Dirac delta pulse, for which $P_R \to \infty$ and $\tau_R \to 0$. In this limiting case, the values of nondimensional peak pressure required to initiate and complete densification become irrelevant (P_R^{init} and P_R^{lim} shown in Fig. 8 are always exceeded), and complete densification can always be achieved for a finite value of the nondimensional reflected impulse I_R. Fig. 12a presents contours with varying mass distribution of the critical nondimensional impulse I_R^{crit} required for complete densification. Note that the contours of I_R^{crit} for the Dirac delta pulse in Fig. 12a are virtually indistinguishable from those for $P_R = 100$ plotted previously in Fig. 9b. Although not plotted herein, it is noted that values of the nondimensional time τ_A required to arrest densification for the Dirac delta pulse are also nearly equivalent to those for $P_R = 100$. (The ratio τ_A/τ_R, plotted for $P_R = 10$ and $P_R = 100$ in Fig. 10, is undefined for the Dirac delta pulse because $\tau_R \to 0$.) The energy dissipation in the core, however, can be significantly larger for the Dirac delta pulse than for $P_R = 100$, as can be observed by comparing the contours of $\widetilde{E}_d/\widetilde{E}_d^{q\text{-}s}$ for the Dirac delta pulse in Fig. 12b with those shown previously for $P_R = 100$ in Fig. 11b. When the mass fraction in the core η_0 approaches unity, the rate-dependent contribution to the energy dissipation can be significantly larger for the Dirac delta pulse than for $P_R = 100$. These observations are consistent with those of Vaziri and Hutchinson (2006) in computational simulations of blast loading on metal sandwich plates, who noted significantly larger energy dissipation when the blast impulse was imparted as an initial velocity to the front face than when it was applied as an exponential pressure pulse, even though the back-face deflections in the two cases were fairly close.

5. Fluid–structure interaction

The analytical model in Section 2 was formulated in terms of the reflected pressure $p_r(t)$, which is influenced by FSI effects. In this section, the approximation developed by Kambouchev et al. (2006) is used to define the reflected pressure $p_r(t)$ corresponding to a specified incident pressure pulse $p_i(t)$, accounting for nonlinear compressibility and FSI effects. For consistency with Kambouchev et al. (2006), an exponential incident pressure pulse is considered, of the form $p_i(t) = p_0 e^{-t/t_0}$, where t_0 is the decay period. Kambouchev et al. (2006) observed that the reflected pressure $p_r(t)$ can also be captured quite well by an exponential pulse, which is con-

veniently expressed as $p_r(t) = p_R e^{-t/t_R}$, where t_R is the decay period of the reflected pulse. The peak reflected pressure p_R is related to the peak incident pressure through the pressure reflection coefficient C_R:

$$C_R \equiv \frac{p_R}{p_0} = 2\frac{7 + 4(p_0/p_A)}{7 + (p_0/p_A)} \tag{42}$$

in which p_A is the ambient air pressure.

The key result of Kambouchev et al. (2006) is an approximation relating the reflected impulse i_R to the incident impulse i_0, which can be expressed as an impulse reflection coefficient α_R:

$$\alpha_R \equiv \frac{i_R}{i_0} \simeq \gamma_R \left(\frac{C_R f_R}{\gamma_R}\right)^{\beta_s/(1+\beta_s)} \beta_s^{\beta_s/(1-\beta_s)} \tag{43}$$

where γ_R and f_R are defined as follows:

$$\gamma_R = 8 - 42\frac{p_A}{p_0}\ln\left(1 + \frac{p_0}{7p_A}\right) \tag{44}$$

$$f_R = \left(6\frac{p_0}{p_A} + 7\right)\sqrt{\frac{(6 + C_R)(p_0/p_A) + 7}{(p_0/p_A + 7)[(1 + 6C_R)(p_0/p_A) + 7][C_R(p_0/p_A) + 7]}} \tag{45}$$

The nondimensional FSI parameter β_s in Eq. (43) is conveniently expressed as

$$\beta_s = \beta_A\left(\frac{7 + 6(p_0/p_A)}{7 + p_0/p_A}\right)\sqrt{\frac{6p_0}{7p_A} + 1} \tag{46}$$

where β_A is an alternative nondimensional parameter introduced by Vaziri and Hutchinson (2006), expressed in terms of ambient air properties:

$$\beta_A = \frac{\rho_A c_A t_0}{m_{FSI}} \tag{47}$$

in which ρ_A is the ambient air density, $c_A = \sqrt{1.4p_A/\rho_A}$ is the ambient speed of sound in air, and m_{FSI} is the areal density of the plate considered in the FSI analysis.

Kambouchev et al. (2006) considered a freestanding solid plate in developing Eq. (43), and further approximations must be introduced in selecting an appropriate value of m_{FSI} to extend this result to a sandwich plate with a crushable core. Vaziri and Hutchinson (2006) considered only the mass of the front face in their analysis of FSI for sandwich plates, i.e., setting $m_{FSI} = m_1$ in Eq. (47). However, they noted that this neglects the resistance due to crushing of the core and thus overestimates the beneficial effects of FSI. In this paper, an alternative approximation is proposed that incorporates the resistance of the core by defining m_{FSI} as the areal density of a solid plate with the same initial acceleration of the front face of the sandwich plate.

Provided that the peak reflected pressure p_R is sufficiently high to initiate densification, the initial acceleration of the front face of the sandwich plate is given by $\ddot{u}_1^{init} = (p_R - \sigma_P)/m_1$. Requiring a corresponding solid plate to have the same initial acceleration under the applied pressure p_R, m_{FSI} can then be defined as $m_{FSI} = p_R/\ddot{u}_1^{init} = m_1/(1 - \sigma_P/p_R)$. If p_R is insufficient to initiate densification, then the sandwich plate responds as a monolithic solid plate and $m_{FSI} = m$. These results can be expressed in terms of nondimensional variables as

$$\eta_{FSI} \equiv \frac{m_{FSI}}{m} = \begin{cases} \eta_1(1 - P_R^{-1})^{-1}, & P_R \geqslant P_R^{init} \\ 1, & P_R < P_R^{init} \end{cases} \tag{48}$$

where η_{FSI} represents the effective mass fraction of the sandwich panel that participates in FSI, and P_R^{init} is defined in Eq. (41). Eq. (48) shows that $\eta_{FSI} \to \eta_1$ as the nondimensional peak pressure P_R becomes large, which corresponds to the approximation used by Vaziri and Hutchinson (2006).

To check the appropriateness of using Eq. (48) to extend FSI results for solid plates to sandwich plates, the acceleration of the solid plate considered in the FSI analysis, denoted $\ddot{u}_{FSI} = p_r(t)/m_{FSI}$, can be compared with the acceleration of the front face of the sandwich panel, given by $\ddot{u}_1 = [p_r(t) - \sigma_P]/[m_1 + \rho_0(\ell_0 - x)]$. With the

exponential reflected pressure pulse $p_r(t) = p_R e^{-t/t_R}$ and with m_{FSI} defined by Eq. (48), the ratio $\ddot{u}_{FSI}/\ddot{u}_1$ can be expressed in terms of nondimensional variables as a product of two factors:

$$\frac{\ddot{u}_{FSI}}{\ddot{u}_1} = \frac{\eta_1 + \eta_0(1-\xi)}{\eta_1} \cdot \frac{1 - P_R^{-1}}{1 - P_R^{-1} e^{\tau/\tau_R}} \tag{49}$$

By definition, $\ddot{u}_{FSI}/\ddot{u}_1 = 1$ initially, but both factors in Eq. (49) increase as time progresses and ξ decreases from unity. The first factor in Eq. (49) is associated with the accretion of crushed core material as the densification front propagates. The resulting increase in inertia may significantly reduce the front-face accelerations if the mass of the front face is small relative to the mass of the core. The second factor in Eq. (49) is associated with the resistance provided by the plateau stress of the core material, which remains constant as the reflected pressure decays. The ratio $\ddot{u}_{FSI}/\ddot{u}_1$ is undefined for $\tau/\tau_R = \ln P_R$, because the plateau stress equals the reflected pressure at this instant, and therefore $\ddot{u}_1 = 0$. For $\tau/\tau_R > \ln P_R$, the plateau stress exceeds the reflected pressure, and the front face decelerates ($\ddot{u}_1 < 0$), provided that the densification front has not already been arrested. Both of these effects (the accretion of crushed core material and the resistance provided by the plateau stress) lead to reduced accelerations of the front face relative to the accelerations of the solid plate considered in the FSI analysis. If such reductions are significant during the period of application of the pressure pulse, then Eq. (48) will overestimate the motion of the front face and thus overestimate the beneficial effects of FSI. Conversely, if the ratio $\ddot{u}_{FSI}/\ddot{u}_1$ remains fairly close to unity during the application of the pressure pulse, then Eq. (48) should be reasonably accurate.

Figs. 13a and b show contours with varying mass distribution of the ratio $\ddot{u}_{FSI}(t_*)/\ddot{u}_1(t_*)$for $P_R = 10$ and $P_R = 100$, respectively. The time t_* is the lesser of the decay period t_R and the arrest time t_A, so that the ratio $\ddot{u}_{FSI}/\ddot{u}_1$ is evaluated at $t = t_R$ unless the densification front is arrested first (see the contours of t_A/t_R in Fig. 10). Note that at $t = t_R$, the reflected pressure has decayed to 36.8% of its initial value, and 63.2 % of the total impulse has been imparted. As in Figs. 10 and 11, the contours in Fig. 13 correspond to complete densification of the core and were computed using the values of I_R^{crit} shown in Fig. 9, with $I_R = 100$ for cases in which complete densification cannot be achieved. When the mass fraction in the core η_0 is small, the ratio $\ddot{u}_{FSI}/\ddot{u}_1$is fairly close to unity for both $P_R = 10$ and $P_R = 100$. However, large values of $\ddot{u}_{FSI}/\ddot{u}_1$ are observed as η_0 approaches unity, particularly when the mass fraction in the front face is small. Much larger values of $\ddot{u}_{FSI}/\ddot{u}_1$ are observed for $P_R = 10$ than for $P_R = 100$, indicating that it is less appropriate in the former case to approximate FSI effects using Eq. (48). This is due largely to the longer decay period associated with the lower level of peak pressure, which allows more time for the accretion of crushed core material during the application of the pressure pulse. For this reason, in the subsequent analysis of FSI effects, numerical results are presented only for the higher level of peak pressure, $P_R = 100$. In addition, the contour for $\ddot{u}_{FSI}(t_*)/\ddot{u}_1(t_*) = 1.5$ in Fig. 13b is

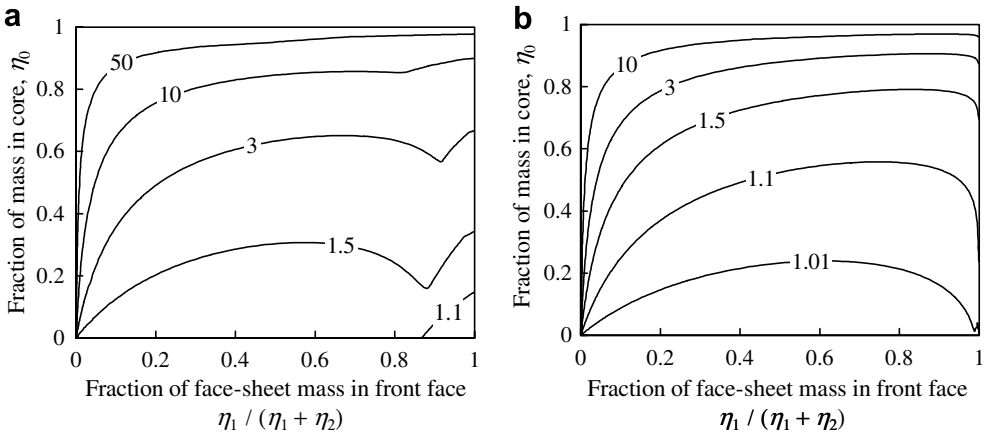

Fig. 13. Contours with varying mass distribution of the ratio $\ddot{u}_{FSI}(t_*)/\ddot{u}_1(t_*)$ between the acceleration of the "equivalent" solid plate used in treatment of FSI and the actual front-face acceleration of the sandwich plate. The time t_* is the lesser of the decay period t_R and the arrest time t_A (see Fig. 10). (a) $P_R = 10$ and (b) $P_R = 100$.

tentatively identified as an approximate limit of applicability of Eq. (48), and in subsequent plots in which FSI effects are considered, the region above this contour is hatched to indicate that the approximation in Eq. (48) is not appropriate. Note that this region corresponds to small values of η_1 and/or large values of η_0, so that the mass of the core is large relative to the mass of the front face.

Implementing the FSI approximations in this section within the analytical model of Section 2 first requires specification of a nondimensional *incident* pressure P_0 and a nondimensional *incident* impulse I_0, defined consistently with the corresponding *reflected* quantities in Eqs. (37) and (26):

$$P_0 = \frac{p_0}{\sigma_P}; \quad I_0 = \frac{i_0}{m}\sqrt{\frac{\rho_0}{\sigma_P \varepsilon_D}} \tag{50a, b}$$

The FSI approximations depend on p_0/p_A, which can be expressed in terms of P_0 as $p_0/p_A = (\sigma_P/p_A)P_0$. In the numerical results presented subsequently, a value of $\sigma_P/p_A = 10$ is considered, which corresponds to a plateau stress of about $\sigma_P = 1$ MPa, as considered previously in the computational simulations. With p_0/p_A thus specified, the pressure reflection coefficient C_R (42) can be evaluated, and the nondimensional peak reflected pressure can be computed as $P_R = C_R P_0$.

It follows from Eqs. (50a,b) that $I_0/P_0 = (t_0/m)\sqrt{\rho_0\sigma_P/\varepsilon_D}$, whereby β_A (47) can be expressed in terms of P_0 and I_0 as

$$\beta_A = \frac{\rho_A c_A}{\sqrt{\rho_0 \sigma_P/\varepsilon_D}} \frac{1}{\eta_{FSI}} \frac{I_0}{P_0} \tag{51}$$

where η_{FSI} can be evaluated from Eq. (48), and a value of the nondimensional constant $\rho_A c_A/\sqrt{\rho_0\sigma_P/\varepsilon_D}$ must be specified from the relevant physical properties. In the numerical results presented subsequently, a value of $\rho_A c_A/\sqrt{\rho_0\sigma_P/\varepsilon_D} = 0.02206$ is considered, which corresponds to setting $\rho_A = 1.225$ kg/m^3 and $c_A = 340.3$ m/s for air and using the values of $\rho_0 = 250$ kg/m^3, $\sigma_P = 1$ MPa, and $\varepsilon_0 = 0.7$ considered previously in the computational simulations. The nondimensional FSI parameter β_s (46) and the impulse reflection coefficient α_R (43) can then be evaluated in terms of p_0/p_A and β_A, whereby the nondimensional reflected impulse can be obtained as $I_R = \alpha_R I_0$. With P_R and I_R thus determined, the response of the sandwich plate can be evaluated by solving the nondimensional equation of motion (25) with the exponential nondimensional reflected pressure pulse in Eq. (39).

Fig. 14a shows contours with varying mass distribution of I_0^{crit}, the nondimensional incident impulse required to produce complete compaction of the core for $P_R = 100$. The values of I_0^{crit} in Fig. 14a are related to the values of I_R^{crit} in Fig. 9b through the impulse reflection coefficient α_R (43): $I_R^{crit} = \alpha_R I_0^{crit}$. Fig. 14b shows

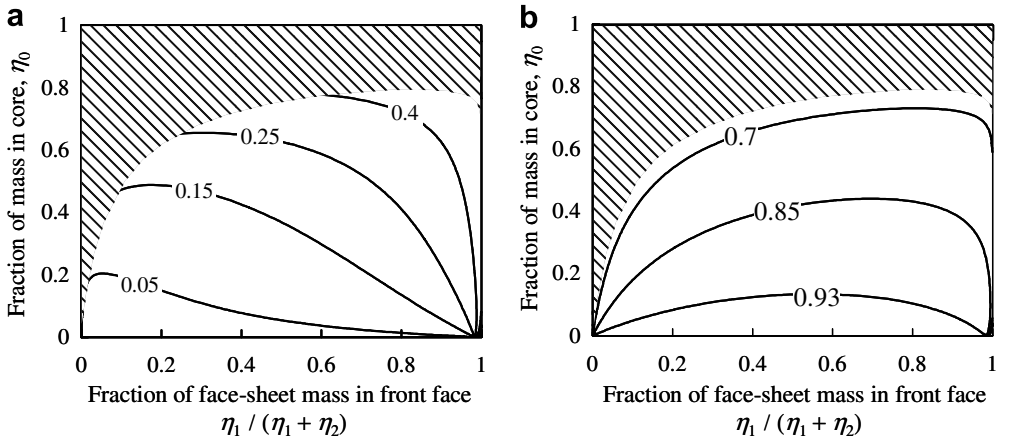

Fig. 14. Contours with varying mass distribution of (a) the nondimensional incident impulse I_0^{crit} required for complete densification of the core and (b) the corresponding ratio α_R/γ_R between the impulse reflected from the sandwich plate and the impulse reflected from a fixed, rigid wall. The approximate treatment of FSI is not applicable in the hatched region, in which $\ddot{u}_{FSI}(t_*)/\ddot{u}_1(t_*) > 1.5$ ($P_R = 100$, $P_0 = 13$, $p_0/p_A = 130$, $\rho_A c_A/\sqrt{\rho_0\sigma_P/\varepsilon_D} = 0.02206$).

corresponding contours of the ratio α_R/γ_R between the impulse reflected from the sandwich plate and the impulse reflected from a fixed, rigid wall for $P_R = 100$. The beneficial effects of FSI are evident in Fig. 14b, with values of α_R/γ_R less than unity indicating impulse reductions due to FSI. Fig. 14b shows a trend of decreasing α_R/γ_R with increasing η_0, with impulse reductions of more than 30 % observed within the domain of applicability of the FSI approximation (48). It is noted that these decreases in α_R/γ_R are associated with underlying increases in the nondimensional FSI parameter β_A (43). Reductions of α_R/γ_R with increasing β_A follow from Eq. (43) and are illustrated in Fig. 1 of Vaziri and Hutchinson (2006). (The ratio α_R/γ_R is equivalent to $I/I_{m_P\to\infty}$ in their notation.)

The increases in β_A that underlie Fig. 14b result from two effects. Firstly, the contours in Fig. 14b correspond to complete densification of the core, with the critical values of incident impulse I_0^{crit} shown in Fig. 14a. Increases in I_0^{crit} then produce increases in β_A, because β_A is proportional to I_0 as shown by Eq. (51). Secondly, decreases in η_1 produce increases in β_A, because β_A is inversely proportional to η_1, according to Eqs. (51) and (48). This latter effect leads to reductions in α_R/γ_R as the fraction of face-sheet mass in the front face $\eta_1/(\eta_1+\eta_2)$ decreases, due to the relatively smaller mass participating in FSI. It is a consequence of this latter effect that the contours of I_0^{crit} in Fig. 14a curve downwards as they approach the hatched region along the left-hand edge of the plot, in contrast with the corresponding contours of I_R^{crit} in Fig. 9b. Further increases in I_0^{crit} may occur in hatched region where $\eta_1/(\eta_1+\eta_2)$ becomes small. However, in the domain of applicability of the FSI approximation (48), I_0^{crit} increases with increasing $\eta_1/(\eta_1+\eta_2)$, and the contours for I_0^{crit} follow the same general trend as those for I_R^{crit} in Fig. 9b.

It is interesting to compare the work done by the pressure pulse with the work done on a corresponding solid plate with the same total mass. For a prescribed reflected pressure pulse $p_r(t)$, Eq. (12) shows that crushing of the cellular core enhances the work done relative to that done on a solid plate due to the increased velocity of the front face. Due to the beneficial effects of FSI, however, $p_r(t)$ is not simply prescribed, but the reflected impulse for a sandwich plate can be reduced by the increase motion of the front face. Combining Eqs. (32a) and (43), the total work done by the pressure pulse on the sandwich plate as a consequence of these competing effects can be expressed as $W_p^{tot} = \widetilde{W}_p^{tot}[\frac{1}{2}(\alpha_R i_0)^2/m]$, where $\widetilde{W}_p^{tot}$ is evaluated by integrating Eq. (34), and the superscript "tot" denotes limiting values as $t\to\infty$. The work done on a solid plate with the same total mass can be expressed as $W_{p,solid}^{tot} = \frac{1}{2}(\alpha_R^{solid} i_0)^2/m$, where α_R^{solid} is evaluated from Eq. (43) with $m_{FSI} = m$ (or $\eta_{FSI} = 1$). The ratio of the work done on the sandwich plate to the work done on the corresponding solid plate can then be expressed as

$$\frac{W_p^{tot}}{W_{p,solid}^{tot}} = \widetilde{W}_p^{tot}\left(\frac{\alpha_R}{\alpha_R^{solid}}\right)^2 \tag{52}$$

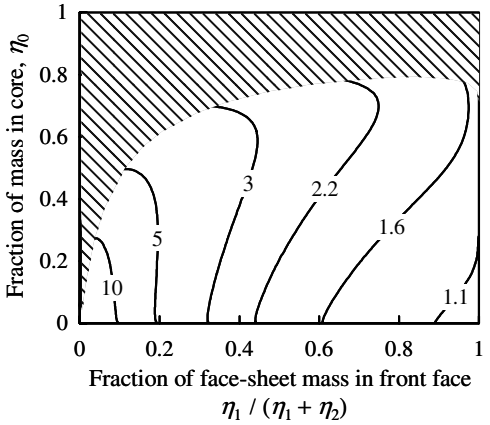

Fig. 15. Contours with varying mass distribution of the ratio $W_P^{tot}/W_{P,solid}^{tot}$ between the work done by the pressure pulse on the sandwich plate and the work done on a solid plate with the same total mass. Values correspond to complete densification of the core, with incident impulses shown in Fig. 14a. The approximate treatment of FSI is not applicable in the hatched region, in which $\ddot{u}_{FSI}(t_*)/\ddot{u}_1(t_*) > 1.5$ ($P_R = 100$, $P_0 = 13$, $p_0/p_A = 130$, $\rho_A c_A/\sqrt{\rho_0\sigma_P/\varepsilon_D} = 0.02206$).

Fig. 15 shows contours with varying mass distribution of the ratio $W_{\mathrm{p}}^{\mathrm{tot}}/W_{\mathrm{p,solid}}^{\mathrm{tot}}$ for $P_{\mathrm{R}} = 100$. As in Fig. 14b, the contours in Fig. 15 correspond to complete densification of the core, with the critical values of incident impulse I_0^{crit} shown in Figs. 14a. All of the values in Fig. 15 are greater than unity, indicating that impulse reductions due to the beneficial effects of FSI are insufficient to offset the enhanced work that results from increased velocities of the front face. Fig. 15 shows that $W_{\mathrm{p}}^{\mathrm{tot}}/W_{\mathrm{p,solid}}^{\mathrm{tot}}$ is largest in the lower left corner of the plot, corresponding to a small mass fraction in the core with most of the mass in the back face. Interestingly, this mass distribution corresponds to the blast pendulum experiments discussed previously, for which simulation results were shown in Fig. 5. Fig. 15 shows that for such mass distributions, the work done by the pressure pulse can be more than ten times larger than the work done on a corresponding solid plate. Increasing the fraction of face-sheet mass in the front face $\eta_1/(\eta_1+\eta_2)$ leads to decreases in $W_{\mathrm{p}}^{\mathrm{tot}}/W_{\mathrm{p,solid}}^{\mathrm{tot}}$.

6. Mitigation of back-face accelerations

The nondimensional back-face acceleration $\tilde{a}_2$, defined in Eq. (31), is an indication of the degree of protection provided by the limiting plateau stress σ_{P} of the cellular core. According to Eq. (31), the peak back-face acceleration occurs when $\xi = 0$ (i.e., at the instant the shock front reaches the back face) and is given by $\tilde{a}_2^{\mathrm{crit}} = \eta_2^{-1}$, while the minimum back-face acceleration occurs when $\xi = 1$ (i.e., at the instant that densification initiates) and is given by $\tilde{a}_2^{\mathrm{init}} = (\eta_0+\eta_2)^{-1}$. Figs. 16a and b show contours of $\tilde{a}_2^{\mathrm{init}}$ and $\tilde{a}_2^{\mathrm{crit}}$, respectively, with varying mass distribution. The two quantities are equivalent in the limit as $\eta_0 \to 0$, but as η_0 increases, $\tilde{a}_2^{\mathrm{init}}$ decreases while $\tilde{a}_2^{\mathrm{crit}}$ increases. For a given mass fraction in the core η_0, increasing the mass fraction in the front face leads to increases in both $\tilde{a}_2^{\mathrm{init}}$ and $\tilde{a}_2^{\mathrm{crit}}$, thus producing larger back-face accelerations.

While the nondimensional back-face acceleration $\tilde{a}_2$ (31) is defined in terms of the plateau stress σ_{P}, an alternative nondimensional back-face acceleration can be defined as $\ddot{u}_2/\ddot{u}_{\mathrm{G}}^{\mathrm{peak}}$, where $\ddot{u}_{\mathrm{G}}^{\mathrm{peak}} = p_{\mathrm{R}}/m$ is the peak acceleration of the center of mass. (This alternative nondimensionalization cannot be used for the Dirac delta pulse, for which $p_{\mathrm{R}} \to \infty$ and thus $\ddot{u}_{\mathrm{G}}^{\mathrm{peak}}$ is undefined.) It follows from Eq. (31) that $\ddot{u}_2/\ddot{u}_{\mathrm{G}}^{\mathrm{peak}} = \tilde{a}_2/P_{\mathrm{R}}$, so that values of $\ddot{u}_2/\ddot{u}_{\mathrm{G}}^{\mathrm{peak}}$ can be obtained from corresponding values of $\tilde{a}_2$ simply through division by the nondimensional peak reflected pressure P_{R}. Using this nondimensionalization, the peak back-face acceleration (at complete densification) can be expressed as $\ddot{u}_2^{\mathrm{crit}}/\ddot{u}_{\mathrm{G}}^{\mathrm{peak}} = \tilde{a}_2^{\mathrm{crit}}/P_{\mathrm{R}} = (\eta_2 P_{\mathrm{R}})^{-1}$. Interestingly, when $\eta_2 < 1/P_{\mathrm{R}}$ (or equivalently, when $\tilde{a}_2^{\mathrm{crit}} > P_{\mathrm{R}}$), the peak back-face acceleration is actually larger than the corresponding peak rigid-body acceleration, thus sacrificing the protective role of the cellular core in limiting the back-face face accelerations. With $P_{\mathrm{R}} = 10$, for example, the contour for $\tilde{a}_2^{\mathrm{crit}} = 50$ in Fig. 12b corresponds to $\ddot{u}_2^{\mathrm{crit}}/\ddot{u}_{\mathrm{G}}^{\mathrm{peak}} = 5$, meaning that the peak back-face acceleration is five times larger than the corresponding rigid-body acceleration.

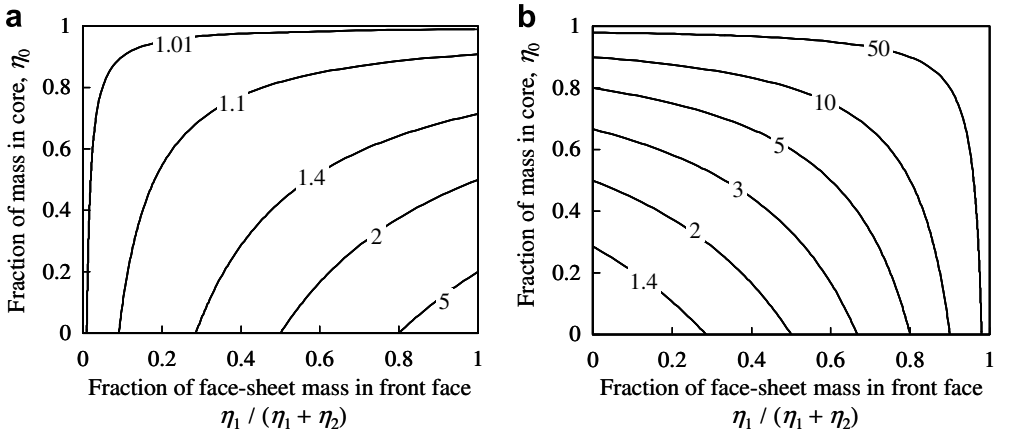

Fig. 16. Contours with varying mass distribution of nondimensional back-face acceleration, $\tilde{a}_2$. (a) At initiation of densification, $\tilde{a}_2^{\mathrm{init}}$ and (b) at complete densification of core, $\tilde{a}_2^{\mathrm{crit}}$.

The plots shown previously in Figs. 8b, 9, 14a, and 15 indicate that for a given mass fraction in the core η_0, increasing the mass fraction in the front face increases the resilience of the system by increasing the nondimensional peak pressure P_R^{lim} and the nondimensional reflected and incident impulses, I_R^{crit} and I_0^{crit}, required for complete densification of the core, and also by reducing the nondimensional work $W_P^{tot}/W_{P,solid}^{tot}$ done by the pressure pulse relative to that done on a corresponding solid plate with the same total mass. However, Fig. 16 indicates that increasing the mass fraction in the front face also leads to increased back-face accelerations, thus sacrificing a protective function of the cellular core. A design optimization problem can then be posed by seeking to determine the distribution of mass that maximizes either the nondimensional reflected impulse I_R or the nondimensional incident impulse I_0 that can be sustained, while limiting the back-face accelerations to a specified maximum value, denoted $\tilde{a}_2^{max}$.

Figs. 17a and b show contour plots with varying mass distribution of, respectively, the maximum nondimensional reflected impulse I_R and the maximum nondimensional incident impulse I_0 that can be sustained with a maximum allowable back-face acceleration of $\tilde{a}_2^{max} = 5$. The values of I_0 in Fig. 17b are related to the values of I_R in Fig. 17a through the impulse reflection coefficient α_R (43), while values of I_0 are not presented in the hatched region of Fig. 17b because the FSI approximation (48) is not appropriate. The plots in Figs. 17a and b can each be divided into three regions in which different conditions prevail. The grey curve in each figure corresponds to the contour for $\tilde{a}_2^{crit} = 5$, plotted previously in Fig. 16b. In the region below the grey curve $\tilde{a}_2^{crit} < 5$, so complete densification of the core can be permitted without exceeding $\tilde{a}_2^{max}$. Therefore, in this region the values of maximum permissible impulse correspond to complete densification of the core, and the contours in Fig. 17a are the same as those for I_R^{crit} in Fig. 9b, while the contours in Fig. 17b are the same as those for I_0^{crit} in Fig. 14a. In the region above the grey curve $\tilde{a}_2^{crit} > 5$, so $\tilde{a}_2^{max}$ will be exceeded if complete densification is allowed. Therefore, the maximum permissible impulses in this region correspond to partial densification of the core and the values in Figs. 17a and b are less than I_R^{crit} and I_0^{crit}, respectively. The shaded region in the lower right-hand corner of Figs. 17a and b is bounded above by the contour for $\tilde{a}_2^{init} = 5$, plotted previously in Fig. 16a. In this region $\tilde{a}_2^{init} > 5$, so $\tilde{a}_2^{max}$ will be exceeded if densification is even allowed to initiate, and thus a nonzero impulse cannot be permitted.

Figs. 17a and b show that the allowable reflected impulse I_R and the allowable incident impulse I_0 both increase monotonically with increasing mass fraction in the core η_0. It can also be observed in Figs. 17a and b that for a given η_0, the allowable values of I_R and I_0 are maximized along the contour for $\tilde{a}_2^{crit} = 5$, shown in grey. This is evident from the fact that the contours of I_R and I_0 attain their minimum values of η_0 along the grey curve, with attendant changes in sign of their slope. Similar results have been observed for other values of the maximum allowable acceleration $\tilde{a}_2^{max}$, and the optimal contour can be expressed more

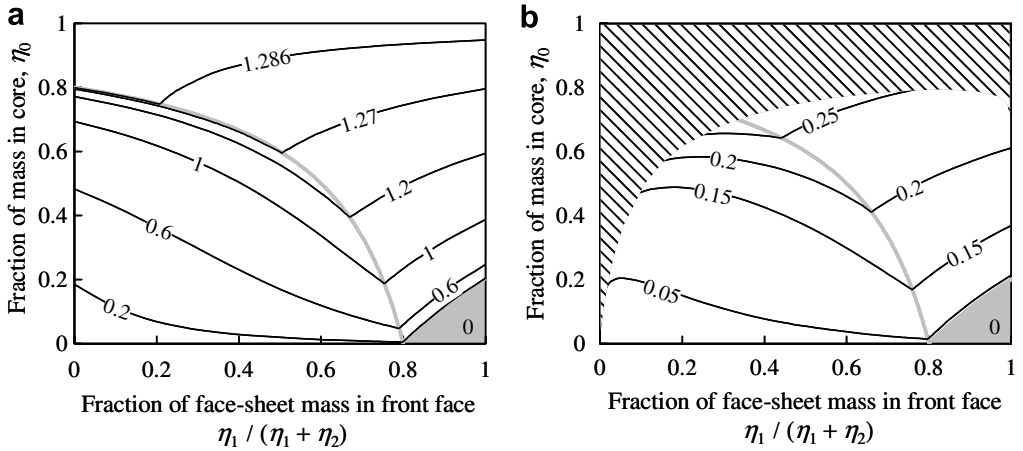

Fig. 17. Contours with varying mass distribution of (a) maximum allowable nondimensional reflected impulse I_R and (b) maximum allowable nondimensional incident impulse I_0 with nondimensional back-face accelerations limited to $\tilde{a}_2^{max} = 5$. The approximate treatment of FSI is not applicable in the hatched region, in which $\ddot{u}_{FSI}(t_*)/\ddot{u}_1(t_*) > 1.5$ ($P_R = 100$, $P_0 = 13$, $p_0/p_A = 130$, $\rho_A c_A/\sqrt{\rho_0 \sigma_P/\varepsilon_D} = 0.02206$).

generally as $\tilde{a}_2^{\text{crit}} = \tilde{a}_2^{\max}$. This means that for a given η_0, the allowable impulse is maximized by adjusting the mass distribution so that the nondimensional acceleration at complete densification, $\tilde{a}_2^{\text{crit}}$, equals the limiting value, $\tilde{a}_2^{\max}$. Noting that $\tilde{a}_2^{\text{crit}} = 1/\eta_2$, this optimal mass distribution can be expressed as $\eta_2 = 1/\tilde{a}_2^{\max}$, which simply corresponds to a constant mass fraction in the back face. For a given η_0, this criterion specifies a mass fraction in the front face of $\eta_1 = 1 - \eta_0 - 1/\tilde{a}_2^{\lim}$, which decreases with increasing η_0 and reduces to zero when $\eta_0 = 1 - 1/\tilde{a}_2^{\max}$. This can be seen in Figs. 13a, in which the contour for $\tilde{a}_2^{\text{crit}} = 5$ intersects the vertical axis at $\eta_0 = 1 - 1/5 = 0.8$. For $\eta_0 > 1 - 1/\tilde{a}_2^{\max}$, the contours of Fig. 13a indicate that the allowable impulse is maximized by placing all of the face-sheet mass in the back face (i.e., setting $\eta_1 = 0$ and $\eta_2 = 1 - \eta_0$). However, it is noted that as η_0 becomes large, the maximum permissible impulse becomes quite insensitive to the relative distribution of mass between the front and back faces. For $\eta_0 = 0.9$, for example, the maximum allowable impulse for $\eta_1/(\eta_1 + \eta_2)$=0.001 is only 0.3% larger than the maximum allowable impulse for $\eta_1/(\eta_1 + \eta_2) = 0.999$.

7. Summary and conclusions

This paper has investigated the uniaxial crushing of a cellular layer sandwiched between solid front and back faces, with air-blast loading applied to the front face and the back-face unrestrained. While previous studies have sought to minimize deflections for sandwich plates with face sheets of equal mass, the objective of the present study was to mitigate shock transmission through the thickness of the sandwich plate, and potential advantages of unequal face sheets were explored by evaluating response characteristics for all possible distributions of mass between the front and back faces and the cellular core. To investigate the crushing response of the system, an analytical model was developed using the well-established rigid, perfectly-plastic, locking (R-P-P-L) idealization for the cellular core. This analytical model represents the propagation of a planar densification front through the core and accounts for the rate-dependent energy dissipation associated with the densification front, which can be many times larger than the quasi-static energy dissipation. Predictions of the analytical model showed excellent agreement with computational simulations using the explicit finite element code LS-DYNA, while a fairly small value of the material viscosity coefficient was required in the computations to avoid additional viscous dissipation due to spreading of the densification front.

Fluid–structure interaction (FSI) effects were treated using a recent result due to Kambouchev et al. (2006) for air-blast loading on solid plates. This result was extended to sandwich plates by defining an "equivalent" solid plate based on the initial acceleration of the front face. This FSI approximation neglects increases in the effective inertia of the front face resulting from accretion of crushed core material as the densification front propagates, and it was found to be inappropriate when the mass fraction in the core η_0 is large relative to the mass in the front face η_1, particularly when the decay period of the pressure pulse is comparable to the propagation time of the densification front. Within its domain of applicability, this approximation relates the nondimensional reflected impulse I_R and the nondimensional peak reflected pressure P_R, which are applied to the front face of the sandwich plate, to the corresponding values I_0 and P_0 associated with the incident air shock.

The capacity of the sandwich plate to mitigate shock transmission is limited by the critical impulse required to produce complete densification of the core, with corresponding nondimensional reflected and incident values denoted I_R^{crit} and I_0^{crit}. For $I_R < I_R^{\text{crit}}$, the cellular core serves a protective function by limiting the stress that reaches the back face to the plateau stress σ_P. For $I_R > I_R^{\text{crit}}$, however, reflection of the densification front from the back-face results in large stresses that can exceed the peak reflected blast pressure by several times. It was observed that I_R^{crit} decreases with increasing nondimensional peak pressure P_R, being smallest in the limiting case of a Dirac delta pulse ($P_R \to \infty$), which corresponds to an initial velocity imparted to the front face. A limiting nondimensional peak pressure $P_R^{\lim}$ was identified, below which only partial densification can be achieved even if the pressure is maintained indefinitely ($I_R^{\text{crit}} \to \infty$), and it was observed that densification of the core cannot initiate if $P_R < (1 - \eta_1)^{-1}$, regardless of the reflected impulse. Values of I_R^{crit} for $P_R = 100$ were virtually indistinguishable from those for the Dirac delta; however, for large η_0, the rate-dependent energy dissipation associated with densification front was many times larger for the Dirac delta pulse.

The influence of mass distribution on the critical impulse was investigated, and it was found that both I_R^{crit} and I_0^{crit} increase with increasing mass fraction in the core η_0. For a given η_0, both I_R^{crit} and I_0^{crit} were found to

increase with increasing mass fraction in the front face η_1, with corresponding decreases in the ratio $W_p^{tot}/W_{p,solid}^{tot}$ of the work done by the pressure pulse on the sandwich plate to the work done on a corresponding solid plate with the same total mass. Impulse reflection coefficients associated with the critical impulses were observed to be reduced by as much as 30% relative to impulse reflection coefficients for a rigid wall, due to the beneficial effects of FSI. In spite of this, the ratio $W_p^{tot}/W_{p,solid}^{tot}$ was always greater than unity, indicating that impulse reductions due to FSI are insufficient to offset the enhanced work that results from increased velocities of the front face. The ratio $W_p^{tot}/W_{p,solid}^{tot}$ is maximized for small values of η_0 and η_1, with most of the mass in the back-face ($\eta_2 \to 1$), for which values of $W_p^{tot}/W_{p,solid}^{tot}$ in excess of 10 are observed, and both I_R^{crit} and I_0^{crit} are also minimized in this region. Interestingly, such mass distributions correspond precisely to the "blast pendulum" experiments of Hanssen et al. (2002), in which impulse enhancement was observed. It is therefore observed that such configurations are particularly well suited for absorbing energy from air blasts and particularly poorly suited for dissipating energy through core crushing, which helps to explain their poor performance for blast mitigation.

The observed increases in I_R^{crit} and I_0^{crit} with corresponding decreases in $W_p^{tot}/W_{p,solid}^{tot}$ suggest that the capacity of the sandwich plate to mitigate shock transmission might be improved by increasing the mass fraction in the front face η_1 and reducing the mass fraction in the back-face η_2. However, it was also observed that reducing η_2 leads to increased back-face accelerations, thus decreasing the protection provided by the core material. In fact, it was found that if $\eta_2 < 1/P_R$, the back-face acceleration can exceed the peak acceleration of the center of mass, meaning that the cellular core actually amplifies the back-face accelerations, rather than reducing them. Motivated by these observations, a design optimization problem was posed that involves finding the mass distribution that maximizes the nondimensional impulse that can be absorbed while limiting the nondimensional back-face accelerations to a specified maximum value, denoted $\tilde{a}_2^{max}$. In the domain of applicability of the FSI approximation, it was found that for a given mass fraction in the core η_0 (provided $\eta_0 < 1 - 1/\tilde{a}_2^{max}$), the allowable values of both I_R and I_0 are maximized by setting the mass fraction in the back face to $\eta_2 = 1/\tilde{a}_2^{max}$. This corresponds to a mass distribution such that the back-face acceleration at complete densification equals the maximum allowable value. While corresponding values of I_0 could not be evaluated for large η_0 due to the inapplicability of the FSI approximation, allowable values of I_R were found to be quite insensitive to the relative distribution of mass between the front and back faces for $\eta_0 > 1 - 1/\tilde{a}_2^{max}$. More detailed computational modeling of FSI effects for sandwich plates would be required to assess whether further increases in the allowable values of I_0 could be achieved when the mass fraction in the front face η_1 is small relative to η_0.

Acknowledgments

This research was supported in part by an appointment of the first author to the Postgraduate Research Participation Program at the US Army Research Laboratory administered by the Oak Ridge Institute for Science and Education through an interagency agreement between the US Department of Energy and USARL. Additional support from USARL through contract 7F013BW208 is gratefully acknowledged.

References

Cooper, G.J., Townend, D.J., Cater, S.R., Pearce, B.P., 1991. The role of stress waves in thoracic visceral injury from blast loading – modification of stress transmission by foams and high-density materials. Journal of Biomechanics 24 (5), 273–285.

Deshpande, V.S., Fleck, N.A., 2005. One-dimensional response of sandwich plates to underwater shock loading. Journal of the Mechanics and Physics of Solids 53, 2347–2383.

Fleck, N.A., Deshpande, V.S., 2004. The resistance of clamped sandwich beams to shock loading. Journal of Applied Mechanics ASME 71, 386–401.

Friend, T., 2005. Using shock wave simulation to optimize body armor. Scientific Computing and Instrumentation.

Hanssen, A.G., Enstock, L., Langseth, M., 2002. Close-range blast loading of aluminum foam panels. International Journal of Impact Engineering 27, 593–618.

Harrigan, J.J., Reid, S.R., Peng, C., 1999. Inertia effects in impact energy absorbing materials and structures. International Journal of Impact Engineering 22, 955–979.

Hutchinson, J.W., Xue, Z., 2005. Metal sandwich plates optimized for pressure impulses. International Journal of Mechanical Sciences 47, 545–569.

Kambouchev, N., Noels, L., Radovitzky, R., 2006. Nonlinear compressibility effects in fluid–structure interaction and their implications on the air-blast loading of structures. Journal of Applied Physics 100 (6), 063519.

Li, Q.M., Meng, H., 2002. Attenuation or enhancement – a one-dimensional analysis on shock transmission in the solid phase of a cellular material. International Journal of Impact Engineering 27, 1049–1065.

Li, Q.M., Reid, S.R., 2006. About one-dimensional shock propagation in a cellular material. International Journal of Impact Engineering 32, 1898–1906.

Lopatnikov, S.L., Gama, B.A., Hauque, M.J., Krauthauser, C., Gillespie, J.W., Guden, M., Hall, I.W., 2003. Dynamics of metal foam deformation during Taylor cylinder – Hopkinson bar impact experiment. Composite Structures 61, 61–71.

Lopatnikov, S.L., Gama, B.A., Hauque, M.J., Krauthauser, C., Gillespie, J.W., 2004. High-velocity plate impact of metal foams. International of Impact Engineering 30, 421–445.

Main, J.A., Gazonas, G.A., 2005. Impulsive loading of cellular media in sandwich construction. In: Proceedings, 14th APS Topical Conference on Shock Compression of Condensed Matter, pp. 1539–1542.

Nesterenko, V.F., 2002. Shock (blast) mitigation by ''soft'' condensed matter. In: MRS Proceedings, vol. 759.

Qiu, X., Deshpande, V.S., Fleck, N.A., 2004. Dynamic response of a clamped circular plate subject to shock loading. Journal of Applied Mechanics ASME 71, 637–645.

Radford, D.D., Deshpande, V.S., Fleck, N.A., 2005. The use of metal foam projectiles to simulate shock loading on a structure. International Journal of Impact Engineering 31, 1152–1171.

Radford, D.D., McShane, G.J., Deshpande, V.S., Fleck, N.A., 2006. The response of clamped sandwich plates with metallic foam cores to simulated blast loading. International Journal of Solids and Structures 43 (7-8), 2243–2259.

Rathbun, H.J., Radford, D.D., Xue, Z., He, M.Y., Yang, J., Deshpande, V., Fleck, N.A., Hutchinson, J.W., Zok, F.W., Evans, A.G., 2006. Performance of metallic honeycomb-core sandwich beams under shock loading. International Journal of Solids and Structures 43 (6), 1746–1763.

Reid, S.R., Peng, C., 1997. Dynamic uniaxial crushing of wood. International Journal of Impact Engineering 19, 531–570.

Tan, P.J., Reid, S.R., Harrigan, J.J., Zou, Z., Li, S., 2005a. Dynamic compressive strength properties of aluminium foams. Part I – experimental data and observations. Journal of the Mechanics and Physics of Solids 53, 2174–2205.

Tan, P.J., Reid, S.R., Harrigan, J.J., Zou, Z., Li, S., 2005b. Dynamic compressive strength properties of aluminium foams. Part II – 'shock' theory and comparison with experimental data and numerical models. Journal of the Mechanics and Physics of Solids 53, 2206–2230.

Taylor, G.I., 1963. The pressure and impulse of submarine explosion waves on plates. In: The Scientific Papers of G.I. Taylor, vol. III. Cambridge University Press, Cambridge, pp. 287–303.

Vaughn, D.G., Canning, J.M., Hutchinson, J.W., 2005. Coupled plastic wave propagation and column buckling. Journal of Applied Mechanics 72, 139–146.

Vaziri, A., Hutchinson, J.W., 2006. Metal sandwich plates subject to intense air shocks. International Journal of Solids and Structures 44, 2021–2035.

Xue, Z., Hutchinson, J.W., 2003. Preliminary assessment of sandwich plates subject to blast loads. International Journal of Mechanical Sciences 45, 687–705.

Xue, Z., Hutchinson, J.W., 2004. A comparative study of impulse-resistant metal sandwich plates. International Journal of Impact Engineering 30, 1283–1305.

Xue, Z., Hutchinson, J.W., 2006. Crush dynamics of square honeycomb sandwich cores. International Journal for Numerical Methods in Engineering 65, 2221–2245.

INTENTIONALLY LEFT BLANK.

NO. OF COPIES	ORGANIZATION
1 (PDF ONLY)	DEFENSE TECHNICAL INFORMATION CTR DTIC OCA 8725 JOHN J KINGMAN RD STE 0944 FORT BELVOIR VA 22060-6218
1	US ARMY RSRCH DEV & ENGRG CMD SYSTEMS OF SYSTEMS INTEGRATION AMSRD SS T 6000 6TH ST STE 100 FORT BELVOIR VA 22060-5608
1	DIRECTOR US ARMY RESEARCH LAB IMNE ALC IMS 2800 POWDER MILL RD ADELPHI MD 20783-1197
1	DIRECTOR US ARMY RESEARCH LAB AMSRD ARL CI OK TL 2800 POWDER MILL RD ADELPHI MD 20783-1197
1	DIRECTOR US ARMY RESEARCH LAB AMSRD ARL CI OK T 2800 POWDER MILL RD ADELPHI MD 20783-1197

ABERDEEN PROVING GROUND

1	DIR USARL AMSRD ARL CI OK TP (BLDG 4600)

NO. OF COPIES ORGANIZATION

1 DPTY ASSIST SCT FOR R&T
SARD TT
ASA (ACT)
J PARMENTOLA
THE PENTAGON RM 3E479
WASHINGTON DC 20310-1714

1 US MILITARY ACADEMY
MATH SCI CTR EXCELLENCE
MADN MATH
THAYER HALL
WEST POINT NY 10996-1786

1 US ARMY MATERIEL CMND
AMCRD
9301 CHAPEK RD
FORT BELVOIR VA 22060-5527

3 AIR FORCE ARMAMENT LAB
AFATL DLJW
W COOK
D BELK
J FOSTER
EGLIN AFB FL 32542

2 DARPA
L CHRISTODOULOU
W COBLENZ
3701 N FAIRFAX DR
ARLINGTON VA 22203-1714

1 US ARMY TACOM ARDEC
AMSTA AR WEE
E BAKER
PICATINNY ARSENAL NJ
07806-5000

2 US ARMY TARDEC
AMSTRA TR R MS 263
K BISHNOI
D TEMPLETON
WARREN MI 48397-5000

3 COMMANDER
US ARMY RESEARCH OFFICE
B LAMATTINA
J LAVERY
D STEPP
PO BOX 12211
RESEARCH TRIANGLE PARK NC
27709-2211

NO. OF COPIES ORGANIZATION

5 DIRECTOR
LANL
P MAUDLIN
R GRAY
W R THISSELL
A ZUREK
F ADDESSIO
PO BOX 1663
LOS ALAMOS NM 87545

1 COMMANDER
US ARMY RSRCH OFC
A RAJENDRAN
PO BOX 12211
RSRCH TRIANGLE PARK NC
27709-2211

7 DIRECTOR
SANDIA NATL LABS
J BISHOP MS 0346
E S HERTEL JR MS 0382
W REINHART MS 1181
T VOGLER MS 1181
L CHHABILDAS MS 1811
M FURNISH MS 1168
M KIPP MS 0378
PO BOX 5800
ALBUQUERQUE NM 87185-0307

1 DIRECTOR
LLNL
M J MURPHY
PO BOX 808
LIVERMORE CA 94550

3 CALTECH
M ORTIZ MS 105 50
G RAVICHANDRAN
T J AHRENS MS 252 21
1201 E CALIFORNIA BLVD
PASADENA CA 91125

5 SOUTHWEST RSRCH INST
C ANDERSON
K DANNEMANN
T HOLMQUIST
G JOHNSON
J WALKER
PO DRAWER 28510
SAN ANTONIO TX 78284

NO. OF COPIES ORGANIZATION

1 TEXAS A&M UNIV
DEPT OF MATH
J WALTON
COLLEGE STATION TX 77843

2 SRI INTERNATIONAL
D CURRAN
D SHOCKEY
333 RAVENSWOOD AVE
MENLO PARK CA 94025

8 UNIV OF NEBRASKA
DEPT OF ENGRG MECH
D ALLEN
F BOBARU
Y DZENIS
G GOGOS
M NEGAHBAN
R FENG
J TURNER
Z ZHANG
LINCOLN NE 68588

1 JOHNS HOPKINS UNIV
DEPT OF MECH ENGRG
K T RAMESH
LATROBE 122
BALTIMORE MD 21218

1 WORCESTER POLYTECHNIC INST
MATH SCI
K LURIE
WORCESTER MA 01609

3 UNIV OF UTAH
DEPT OF MATH
A CHERKAEV
E CHERKAEV
T FOLIAS
SALT LAKE CITY UT 84112

1 PENN STATE UNIV
DEPT OF ENGNG SCI & MECH
F COSTANZO
UNIV PARK PA 168023

2 UNIV OF DELAWARE
DEPT OF MECH ENGRG
T BUCHANAN
T W CHOU
126 SPENCER LAB
NEWARK DE 19716

NO. OF COPIES ORGANIZATION

2 UNIV OF DELAWARE
CTR FOR COMPOSITE MTRLS
J GILLESPIE
M SANTARE
126 SPENCER LAB
NEWARK DE 19716

1 COMPUTATIONAL MECHS CONSLNT
J A ZUKAS
PO BOX 11314
BALTIMORE MD 21239-0314

1 KAMAN SCI CORP
D L JONES
2560 HUNTINGTON AVE STE 200
ALEXANDRIA VA 22303

1 APPLIED RSCH ASSOC
D E GRADY
4300 SAN MATEO BLVD NE
STE A220
ALBUQUERQUE NM 87110

6 INST OF ADVANCED TECH
UNIV OF TX AUSTIN
S BLESS
H FAIR
D LITTLEFIELD
C PERSAD
P SULLIVAN
S SATAPATHY
3925 W BRAKER LN
AUSTIN TX 78759-5316

1 INTRNTL RSRCH
ASSOC INC
D L ORPHAL
4450 BLACK AVE
PLEASANTON CA 94566

1 AKT MISSION RSRCH CORP
M EL RAHEB
23052 ALCALDE DR
LAGUNA HILLS CA 92653

1 WASHINGTON ST UNIV
SCHOOL OF MECHL
AND MTRL ENGRG
J L DING
PULLMAN WA 99164-2920

NO. OF COPIES ORGANIZATION

2 WASHINGTON ST UNIV
INST OF SHOCK PHYSICS
Y M GUPTA
J ASAY
PULLMAN WA 99164-2814

1 ARIZONA STATE UNIV
MECHL AND AEROSPACE ENGRG
D KRAJCINOVIC
TEMPE AZ 85287-6106

1 NORTHWESTERN UNIV
DEPT OF CIVIL & ENVIRON ENGRG
Z BAZANT
2145 SHERIDAN RD
EVANSTON IL 60208-3109

1 UNIV OF DAYTON RSRCH INST
N S BRAR
300 COLLEGE PARK
MS SPC 1911
DAYTON OH 45469

2 TEXAS A&M UNIV
DEPT OF GEOPHYSICS
F CHESTER
T GANGI
COLLEGE STATION TX 77843

1 UNIV OF SAN DIEGO
DEPT OF MATH & CMPTR SCI
A VELO
5998 ALCALA PARK
SAN DIEGO CA 92110

1 NIST
BLDG & FIRE RSRCH LAB
J MAIN
100 BUREAU DR MS 8611
GAITHERSBURG MD 20899-8611

1 MIT
DEPT ARNT ASTRNTC
R RADOVITZKY
77 MASSACHUSETTS AVE
CAMBRIDGE MA 02139

2 MTRLS SCI CORP
A CAIAZZO
R LAVERTY
181 GIBRALTAR RD
HORSHAM PA 19044

NO. OF COPIES ORGANIZATION

2 DIR USARL
AMSRD ARL D
C CHABALOWSKI
V WEISS
2800 POWDER MILL RD
ADELPHI MD 20783-1197

ABERDEEN PROVING GROUND

77 DIR USARL
AMSRD ARL WM
S KARNA
J MCCAULEY
P PLOSTINS
J SMITH
T WRIGHT
AMSRD ARL WM B
J NEWILL
M ZOLTOSKI
AMSRD ARL WM BA
D LYON
AMSRD ARL WM BC
P WEINACHT
AMSRD ARL WM BD
P CONROY
B FORCH
R LIEB
R PESCE-RODRIGUEZ
B RICE
AMSRD ARL WM BF
W OBERLE
AMSRD ARL VT RP
J BORNSTEIN
AMSRD ARL WM M
R DOWDING
S MCKNIGHT
AMSRD ARL WM MA
R JENSEN
A RAWLETT
M VANLANDINGHAM
E WETZEL
AMSRD ARL WM MB
M BERMAN
L BURTON
T BOGETTI
M CHOWDHURY
W DE ROSSET
W DRYSDALE
A FRYDMAN
D HOPKINS
L KECSKES
T H LI
M MINNICINO

NO. OF COPIES	ORGANIZATION
	B POWERS
	J TZENG
	AMSRD ARL WM MC
	R BOSSOLI
	S CORNELISON
	M MAHER
	W SPURGEON
	AMSRD ARL WM MD
	B CHEESEMAN
	E CHIN
	K CHO
	B DOOLEY
	C FOUNTZOULAS
	G GAZONAS
	J LASALVIA
	P PATEL
	J SANDS
	B SCOTT
	C F YEN
	AMSRD ARL WM SG
	T ROSENBERGER
	AMSRD ARL WM T
	P BAKER
	AMSRD ARL WM TA
	M BURKINS
	AMSRD ARL WM TB
	N ELDREDGE
	J STARKENBERG
	AMSRD ARL WM TC
	R COATES
	T FARRAND
	K KIMSEY
	M FERMEN-COKER
	D SCHEFFLER
	S SCHRAML
	S SEGLETES
	AMSRD ARL WM TD
	S BILYK
	T BJERKE
	D CASEM
	J CLAYTON
	D DANDEKAR
	M GREENFIELD
	B LOVE
	M RAFTENBERG
	E RAPACKI
	M SCHEIDLER
	T WEERASOORIYA
	AMSRD ARL WM TE
	J POWELL
	B RINGERS
	G THOMSON
	AMSRD ARL WM UV
	D WILKERSON

INTENTIONALLY LEFT BLANK.